

SYNTHESIS AND CHARACTERIZATION OF TiO<sub>2</sub> NANOTUBE  
SCHOTTKY DIODES

---

A Thesis  
presented to the  
Faculty of the Graduate School  
at the University of Missouri–Columbia

---

In Partial Fulfillment  
Of the Requirements for the Degree  
Master of Science

---

By  
MACH ROBERT MICHAELS  
Dr. Jae W. Kwon, Thesis Supervisor

May 2021

The undersigned, appointed by the Dean of the Graduate School, have examined the  
thesis entitled

SYNTHESIS AND CHARACTERIZATION OF TiO<sub>2</sub> NANOTUBE  
SCHOTTKY DIODES

presented by Mach Robert Michaels,

a candidate for the degree of  
Master of Science

and hereby certify that, in their opinion, it is worthy of acceptance.

---

Dr. Jae W. Kwon

---

Dr. Scott Kovaleski

---

Dr. Ping Yu

## ACKNOWLEDGEMENTS

I would first like to express my gratitude to my advisor, Dr. Jae W. Kwon, for his expertise, support, and encouragement to continuously learn. As an undergraduate, he provided me with the invaluable opportunity to explore my interests in device fabrication and without Dr. Kwon's support, this work would not have been possible. I would also like to thank my thesis committee members Dr. Scott Kovaleski, and Dr. Ping Yu for their insightful contributions towards my work. I want to give a special thanks to my partner, family, and friends for their loving support and encouragement. And finally, I would like to recognize my colleagues Dr. Quang Nguyen, Dilip Venugopal, Eric Acosta, Richard Barber, Ryan McCay, and Nanda Kasani as it was a blast working with all of you over the past two years.

# TABLE OF CONTENTS

<b>ACKNOWLEDGEMENTS .....</b>	<b>ii</b>
<b>TABLE OF CONTENTS .....</b>	<b>iii</b>
<b>LIST OF FIGURES.....</b>	<b>v</b>
<b>LIST OF TABLES.....</b>	<b>viii</b>
<b>NOMENCLATURE .....</b>	<b>ix</b>
<b>ABSTRACT.....</b>	<b>xi</b>
<b>1 INTRODUCTION.....</b>	<b>1</b>
1.1 Scope of this Thesis .....	2
1.2 Thesis Organization .....	2
<b>2 BACKGROUND.....</b>	<b>5</b>
2.1 Semiconductors.....	5
2.1.1 Semiconductor Materials.....	7
2.1.2 Titanium Dioxide .....	8
2.2 Metal-Semiconductor Contacts.....	11
<b>3 METHODS.....</b>	<b>15</b>
3.1 Fabrication .....	15
3.1.1 Electrochemical Anodization .....	15
3.1.2 Heat Treatment.....	18
3.1.3 Sputter Deposition.....	19
3.1.4 Atomic Layer Deposition .....	20
3.2 Characterization .....	23
3.2.1 X-Ray Diffraction .....	23
3.2.2 Ultraviolet-Visible Spectroscopy .....	23
3.2.3 Scanning Electron Microscopy .....	24
3.2.4 Current-Voltage and Capacitance-Voltage .....	26
3.2.5 Numerical Methods.....	29

<b>4</b>	<b>RESULTS.....</b>	<b>31</b>
4.1	Crystal Structure Analysis using XRD .....	31
4.2	Surface and Cross-Sectional Analysis using SEM .....	32
4.3	Elemental Composition using EDX and Backscatter Imaging .....	38
4.4	UV-Vis Spectrum.....	42
4.5	Current – Voltage Characteristics .....	42
4.6	Capacitance – Voltage Characteristics .....	50
<b>5</b>	<b>CONCLUSION &amp; FUTURE WORK.....</b>	<b>51</b>
5.1	Conclusion .....	51
5.2	Future Work .....	52
	<b>APPENDIX.....</b>	<b>54</b>
I.	Reverse Saturation Current Density .....	54
II.	Linear Least-Squares Regression Algorithm.....	55
	<b>REFERENCES .....</b>	<b>56</b>

## LIST OF FIGURES

Figure 2-1: Band structure for solid insulators, semiconductors, and conductors.....	5
Figure 2-2: Fermi-Dirac distribution function of electron energies at given temperatures.	6
Figure 2-3: Illustration of the anatase crystal structure of TiO <sub>2</sub> with lattice parameters a=3.782 Å and c=9.502 Å.....	8
Figure 2-4: Band diagram of TiO <sub>2</sub> .....	9
Figure 2-5: Illustration of oxygen vacancies in an anatase TiO <sub>2</sub> supercell.....	10
Figure 2-6: Illustration of (a) a Schottky and (b) ohmic contact with an n-type semiconductor and their (c-d) corresponding electron energy band diagrams at thermal equilibrium.....	11
Figure 2-7: Ideal diode J-V characteristics where the ideality factor $\eta=1$ . ....	13
Figure 2-8: Illustration of the (a) forward and (b) reverse bias mechanism for a rectifying metal contact on n-type semiconductors.....	14
Figure 3-1: Design of a conformal TiO <sub>2</sub> -NT Schottky diode. ....	15
Figure 3-2: Configuration to electrochemically fabricate double sided TiO <sub>2</sub> -NTs. ....	17
Figure 3-3: Illustration of the two-step anodization process on (a) a thin Ti foil. Initial anodization (b) forms a compacted TiO <sub>2</sub> layer before (c) forming a randomly arranged porous structure. (d) Pores are ultrasonically removed, leaving behind a surface pattern for the (e) second anodization step. ....	18
Figure 3-4: Tube furnace for high temperature annealing.....	18
Figure 3-5: RF sputter deposition chamber. ....	20
Figure 3-6: Typical ALD process cycle for Pt film growth.....	21
Figure 3-7: The modes of ALD deposition into porous structures where (a) a conformal deposition occurs in a reaction-limited condition, (b) partial surface coverage for diffusion-limited modes, and (c) an uneven deposition rate towards the bottom of the nanostructure in recombination-limited modes. ....	22

Figure 3-8: (a) Annealed TiO <sub>2</sub> sample with a protective Au layer and (b) after Pt-ALD with the Au layer removed.....	22
Figure 3-9: FEI Quanta 600 FEG Environmental SEM.....	25
Figure 3-10: Operational overview of an EDS detector. ....	26
Figure 3-11: (a) Keithley 2601A Source Meter for Current-Voltage measurements and (b) an HP 4279 C-V meter for Capacitance-Voltage measurements.....	29
Figure 4-1: X-ray diffraction patterns of TiO <sub>2</sub> -NTs annealed at 450°C, 550°C, and 750°C. ....	31
Figure 4-2: X-ray diffraction patterns of a Ti foil, TiO <sub>2</sub> film, and TiO <sub>2</sub> -NTs annealed at 550°C. ....	32
Figure 4-3: Initial anodization trial where the surface of the NTs exhibited (a) a collapse in the porous structure and (b) developed random particle features after thermal annealing. ....	32
Figure 4-4: Backscatter image of the initial anodization parameters. ....	33
Figure 4-5: 15-minute anodization time where (a) pores are clearly visible but (b) a large-scale distribution of unwanted nanoscale features remained on the surface. ....	33
Figure 4-6: (a) 10-minute anodization where surface features are removed, however, (b) subsurface cracks are found throughout the structure using backscatter imaging.....	34
Figure 4-7: (a) 3-minute anodization with an annealing temperature ramping rate of 3°C/min along with the (b) cross-sectional area with NT length of about 625 nm. ....	35
Figure 4-8: (a) Surface pattern left behind after a 1-hour ultrasonic cleaning and the (b) Pt coated porous TiO <sub>2</sub> structure formed after a 2 <sup>nd</sup> anodization step. ....	36
Figure 4-9: SEM image of the Pt/TiO <sub>2</sub> surface with a corresponding Fast Fourier Transform.....	36
Figure 4-10: Average pore diameter analysis. ....	37
Figure 4-11: Circularity ratio and average pore perimeter. ....	37
Figure 4-12: NT growth rate vs. Anodization time.....	38

Figure 4-13: EDX analysis of the cross-sectional area of a 625 nm long NT. ....	39
Figure 4-14: (a) Secondary and (b) backscatter electron images showing low density areas indicating a diffusion-limited deposition regime.....	39
Figure 4-15: Discontinuous Pt deposition at the bottom of the NTs. ....	40
Figure 4-16: The (a) cross section of the Pt/TiO <sub>2</sub> -NT array with a (b-d) corresponding elemental composition map for Pt, Ti, and O. ....	41
Figure 4-17: UV-vis spectrum of stoichiometric and nonstoichiometric TiO <sub>2</sub> -NTs. ....	42
Figure 4-18: Resistance in the electrolyte increases during the anodization process for one minute before slowly decreasing at 3.3 mΩ/min as Ti ions enter the solution.....	43
Figure 4-19: (a) Current-Voltage characteristics of stoichiometric TiO <sub>2</sub> -NT Schottky diodes for the as-deposited Pt and thermally treated diodes. (b) Semi-log plot with corresponding ideality factors.....	43
Figure 4-20: (a) Current-Voltage characteristics of nonstoichiometric TiO <sub>2</sub> -NT Schottky diodes for the as-deposited Pt and thermally treated diodes. (b) Semi-log plot with corresponding ideality factors and fitted curve (blue). ....	44
Figure 4-21: Equivalent circuit with a parallel, or shunt, conduction path.....	45
Figure 4-22: Norde's method plot F(V)-V for both stoichiometric and nonstoichiometric TiO <sub>2</sub> -NT diodes.....	45
Figure 4-23: Cheung and Cheung's functions plotted for (a) stoichiometric and (b) nonstoichiometric TiO <sub>2</sub> -NT diodes.....	46
Figure 4-24: Log-Log plot for both stoichiometric and nonstoichiometric TiO <sub>2</sub> -NT diodes. ....	47
Figure 4-25: Forward bias J-V and G-V curves for (a) stoichiometric and (b) nonstoichiometric samples. G-V characteristics represent the transition voltage between the trap-limited and SCLC regions. ....	49
Figure 4-26: Capacitance-Voltage measurements of as-deposited and post-thermally treated stoichiometric and nonstoichiometric TiO <sub>2</sub> -NT Schottky diodes. ....	50



## LIST OF TABLES

Table 2-1: Metal work functions for common semiconductor contacts. ....	12
Table 3-1: Scalar quantities for the volume of ethylene glycol (mL) needed for a given wt% NH <sub>4</sub> F and vol% water. ....	16
Table 3-2: Scalar quantities for the volume of deionized water (mL) needed for a given wt% NH <sub>4</sub> F and vol% water. ....	16
Table 4-1: Calculated cylindrical surface area, the number of pores per area, and the overall aspect ratio. ....	37
Table 4-2: Mass % of elements found under different annealing conditions. ....	41
Table 4-3: As deposited Pt/TiO <sub>2</sub> -NT Schottky diodes. ....	46
Table 4-4: Post-thermal treatment Pt/TiO <sub>2</sub> -NT Schottky diodes. ....	47
Table 4-5: Slopes in each region of the log-log plot. ....	48

## NOMENCLATURE

ALD	atomic layer deposition	-
C-V	capacitance - voltage	-
$E_a$	applied voltage	[V]
$\epsilon_0$	permittivity of free space	$8.85 \times 10^{-14}$ [F/cm]
$\epsilon_r$	relative permittivity	[F/cm]
EDX	energy-dispersive x-ray spectroscopy	-
$E_F$	Fermi energy	[eV]
h	Planck's constant	$4.136 \times 10^{-15}$ [eV · s]
-	-	$6.626 \times 10^{-34}$ [J · s]
I-V	current - voltage	-
J	electric current density	[A/cm <sup>2</sup> ]
$J_0$	reverse-biased saturation current density	[A/cm <sup>2</sup> ]
$k_B$	Boltzmann's constant	$8.617 \times 10^{-5}$ [eV/K]
-	-	$1.381 \times 10^{-23}$ [J/K]
$m^*$	effective mass	[kg]
M-S	metal-semiconductor	-
$\eta$	ideality factor	-
$\phi_{sb}$	Schottky barrier	[eV]
$\phi_m$	metal work function	[eV]
q	electron charge	$1.602 \times 10^{-19}$ [C]

SCLC	space charge limited current	-
SEM	scanning electron microscope	-
TiO <sub>2</sub>	titanium dioxide	-
$V_t = \frac{k_B T}{q}$	thermal voltage	25.86 [mV] at 300K
vol%	volume percent	[mL]
wt%	weight percent	[g]
$\chi$	electron affinity	[eV]
XRD	x-ray diffraction	-

# SYNTHESIS AND CHARACTERIZATION OF TiO<sub>2</sub> NANOTUBE SCHOTTKY DIODES

Mach R. Michaels

Dr. Jae W. Kwon, Thesis Supervisor

## ABSTRACT

Metal-semiconductor interfaces on one-dimensional (1D) nanostructures represent crucial building blocks for next-generation nanoelectronics. Over the past two decades, chemically synthesized titanium dioxide nanotubes (TiO<sub>2</sub>-NTs) have gained a considerable amount of interest due to their high specific surface areas, tunable geometries, and favorable electrical properties. Explored for a variety of applications such as solar cells, hydrogen production, memristors, and batteries, TiO<sub>2</sub> is a transition metal oxide material that contains unique wide-bandgap semiconductor properties.

This research seeks to fabricate a conformal, rectifying metal-semiconductor interface, or Schottky junction, throughout an ordered array of semiconducting nanotubes. The atomic layer deposition (ALD) technique offers a precise, conformal growth mechanism and was used to deposit a continuous platinum (Pt) Schottky contact throughout the inner walls of the TiO<sub>2</sub>-NTs. Any defects found in the nanotubes, such as cracks, led to Pt atoms reaching all areas, forming an electrical short between the anode and cathode. To address this issue, initial experiments were centered on synthesizing defect-free, ordered TiO<sub>2</sub>-NT arrays using electrochemical anodization as it offers precise geometric control over the NT growth. Fabrication parameters, such as anodization time, electrolyte concentrations, and annealing environments, were investigated until the resulting NTs were free from structural defects.

Demonstrated with low vacuum annealing, oxygen vacant, nonstoichiometric TiO<sub>2</sub> was synthesized and investigated as a diode material. By comparing the current-voltage characteristics between stoichiometric and nonstoichiometric TiO<sub>2</sub> diodes, we find that the oxygen vacant, nonstoichiometric TiO<sub>2</sub> diodes displayed an improved ideality factor from 3.7 to 2.4. A 350°C post-fabrication thermal treatment, however, led to both stoichiometric and nonstoichiometric TiO<sub>2</sub> diodes having similar ideality factors of 2.0 and similar shifts in trap concentration and depth. Nonstoichiometric TiO<sub>2</sub> devices exhibited a unique shunt conduction regime after thermal treatment where the shunt resistance was found to be on the order of 10<sup>5</sup> Ω. These results present valuable experimental observations into understanding the effects of oxygen vacancies in TiO<sub>2</sub> and effectively modifying the electronic properties of a conformal Pt/TiO<sub>2</sub> nanostructured junction using a facile post-fabrication thermal treatment.

# 1 INTRODUCTION

Nanoscience and nanotechnology are cutting-edge areas of research that continue to find novel roles in scientific fields such as biomedical, chemical, computational, engineering, and physics. In order to miniaturize existing technologies and create a new, this technology seeks to manipulate the unique physical and electrical properties of nanoscale materials, or nanomaterials. Nanomaterials range in size from about 1 to 100 nm and can be categorized by their dimensionality. Since the development of one-dimensional (1D) carbon nanotubes (NTs),<sup>1</sup> nanostructure materials experienced an exponential increase in research interest due to their high specific surface area and surface-to-volume ratios. This ratio dramatically increases as the nanomaterial reduces in size. At nanoscale, many innate material properties emerge which need to be accounted for, whereas in bulk materials these characteristics are negligible. These properties include mechanical and thermal properties, electrical and magnetic characteristics, and the surface activity and reactivity.

Oxide semiconductors such as titanium dioxide ( $\text{TiO}_2$ ) have shown promising electrical characteristics as thin nanostructured films. Semiconductor devices make use of a number of heterojunctions, such as metal-semiconductor (M-S) interfaces, to perform application specific tasks. The reproduction of this interface requires a comprehensive understanding of semiconductor properties and the unique behaviors exhibited when in contact with certain metals.

## **1.1 Scope of this Thesis**

Nanostructures provide a pathway for electronics continue to reduce in size while maintaining, or improving upon, device performance. The ability to form a conformal heterojunction on nanostructured semiconductors, however, remains a technological challenge. Conventional deposition methods for metal contacts include magnetron sputter, electroplating, or thermal evaporation and have previously been used as contact barriers for NT structures. However, at nanoscale, these methods only offer a non-uniform pore coverage, consequently failing to utilize the high specific surface area that NTs offer. This thesis seeks to develop a conformal Schottky barrier throughout self-organized stoichiometric and nonstoichiometric TiO<sub>2</sub>-NTs. These highly ordered TiO<sub>2</sub>-NT arrays are synthesized using an electrochemical anodization method and subsequently coated with platinum using atomic layer deposition to establish a conformal Schottky barrier. This study presents the nanostructure properties, fabrication techniques, and the electrical properties and behavior of stoichiometric and nonstoichiometric TiO<sub>2</sub>-NT diodes. The reader will be introduced to semiconductor concepts and materials, the nanofabrication processes, and characterization techniques.

## **1.2 Thesis Organization**

The research presented in this thesis is organized into five chapters. Following this introduction, Chapter 2 introduces the fundamentals of semiconductors, semiconductor materials, and the behavior between metal-semiconductor contacts. This chapter provides a brief classification of semiconductors and a necessary introduction to band theory using Fermi-Dirac statistics and, briefly, the conduction mechanism when an electric field is applied. Also introduced is an overview of oxide semiconductors and the material used

throughout this thesis, titanium dioxide. Details regarding  $\text{TiO}_2$  are presented in this section reviewing the stoichiometric and nonstoichiometric crystal structure, band diagram, and the applications in which nanostructured  $\text{TiO}_2$  has played a role.

Chapter 3 describes the methods used to create and characterize the nanostructured Schottky diode. In the first part of this chapter, the fabrication process is explained in detail reviewing the electrochemical process and crystallization of the resulting amorphous materials. This section reviews two material deposition processes used to create sacrificial layers and contact electrodes. Characterization techniques are also discussed in this chapter reviewing the atomic and nanostructure analysis methods, electrical measurements used, and the numerical linear approximations used to extract electrical parameters from the diode.

In chapter 4, the results and analysis of this study reveal the surface and crystal structure, the quality of the metal contact deposition, as well as the current-capacitance-voltage characteristics for both stoichiometric and nonstoichiometric  $\text{TiO}_2$ -NT diodes. Electrochemical parameters such as the applied potential, anodization time, fluorine and water concentration, and a 1-vs-2 step anodization were varied in this study and examined via imaging data. Crystallization parameters were also varied such as the annealing environment, temperatures, and the temperature ramping rates to analyze the crystal and surface structure changes. Environmental parameters include atmospheric, pure  $\text{O}_2$ , and vacuum environment. The rate at which the temperature increased and decreased was modified to analyze the effects of ramping rates on surface defects such as crack formation and propagation. Lastly, the electrical characteristics are presents in this chapter where parameters such as the ideality factor, Schottky barrier height, and series resistances are



gathered from current-voltage measurements. The capacitance-voltage measurements are also briefly examined in this study.

Finally, chapter 5 summarizes the results of this study and proposes the promising future direction for this work.

## 2 BACKGROUND

### 2.1 Semiconductors

Good insulators have resistivity values as large as  $10^{22}$   $\Omega$ -cm while a typical conductor averages around  $10^{-6}$   $\Omega$ -cm. At  $T = 0\text{K}$ , semiconductors are perfect insulators, however, as the temperature increases the resistivity decreases resulting in conduction.<sup>2</sup> Alternatively, these solids can be characterized by the energy gap, or bandgap, between the conduction and valence bands as shown in Figure 2-1. It is important to consider whether the semiconductor has a direct or indirect bandgap by viewing the energy curves of both bands in “ $k$ -space.” If both the valence and conduction band have maximum and minimum energies, respectively, that lie on the same wavevector,  $k$ , then the semiconductor has a direct bandgap. However, if they have misaligned wavevectors, then the semiconductor

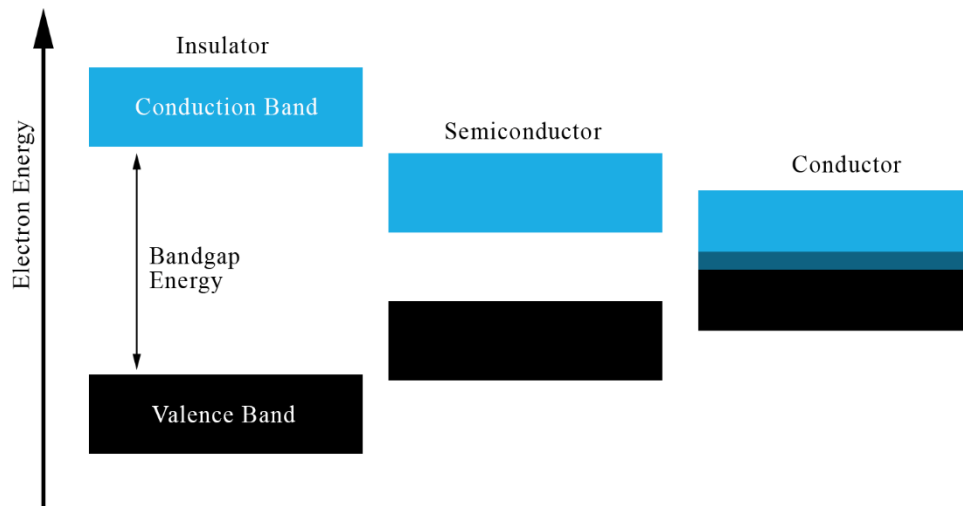


Figure 2-1: Band structure for solid insulators, semiconductors, and conductors.

has an indirect bandgap.<sup>3</sup> Conduction occurs in a semiconductor when electrons are thermally excited across the bandgap, this mechanism results in an unoccupied level, or an electron hole in the valence band. The electrical conductivity rapidly increases as a function

of temperature and can be further improved by introducing substitutional or interstitial impurities.<sup>4</sup> These dopants add to either the donor or acceptor concentration by supplying additional electrons to the conduction band or additional holes to the valence band, respectively. The change in impurity concentration reduces the amount of energy required to move an electron into the conduction band or hole from the valence band.

If a system is in thermal equilibrium, the Fermi-Dirac distribution function can be used to determine the number of existing quantum states at energy,  $E$ , that are either occupied or empty. The Fermi-Dirac distribution function,  $f$ , is defined as

$$f(E) = \frac{1}{\exp\left(\frac{E - E_F}{k_B T}\right) + 1} \quad (2.1)$$

where  $E_f$ ,  $k_B$ , and  $T$  are denoted as the Fermi level, Boltzmann constant, and absolute temperature, respectively.<sup>3</sup> Figure 2-2 shows this distribution at various temperatures as a function of the electron energy relative to the Fermi level. In semiconductors, the number of electrons,  $n_c$ , in the conduction band and the number of holes,  $p_v$ , in the valence band

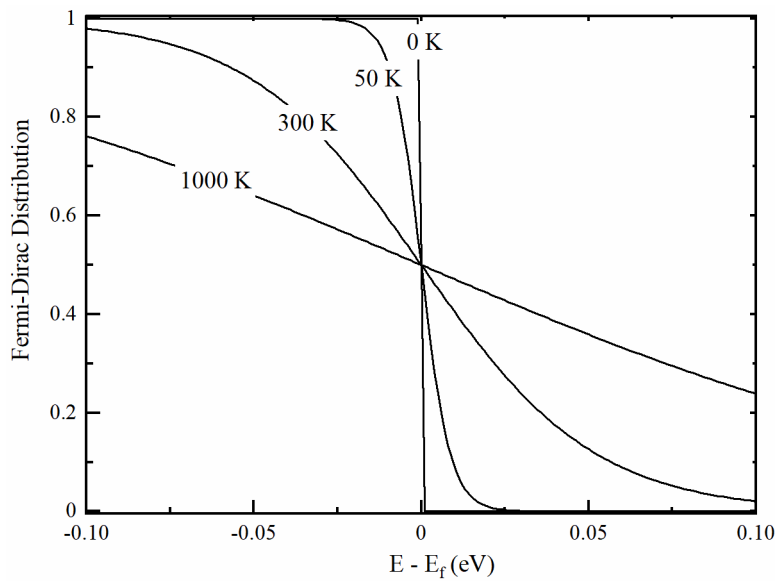


Figure 2-2: Fermi-Dirac distribution function of electron energies at given temperatures.

can be determined using the Fermi-Dirac statistics at any temperature  $T$  and is given by

$$n_c(T) = \int_{E_c}^{\infty} dE D_c(E) f(E) \quad (2.2)$$

$$p_v(T) = \int_{-\infty}^{E_v} dE D_v(E) (1 - f(E)) \quad (2.3)$$

where  $D(E)$  is the number of states with energies between  $(E, E + dE)$  per unit volume, or the density of states.

Under an applied electric field, the electrons and holes experience a force in opposite directions such that they produce a net acceleration in the direction of the conduction and valence bands, respectively. This drift current density in a semiconductor material is given by

$$J = \sigma E_a \quad (2.4)$$

where  $\sigma$  and  $E_a$  is defined as the conductivity (reciprocal of resistivity) and the applied voltage. The mobility values of electrons,  $\mu_n$ , and holes,  $\mu_p$ , contribute to the overall conductivity and is expressed as the following.

$$\sigma = q \cdot (\mu_n n + \mu_p p) \quad (2.5)$$

### 2.1.1 Semiconductor Materials

Semiconductor materials can be classified as single crystal, polycrystalline, and amorphous. Single crystals such as silicon have well-defined geometric arrangements in their atomic structure, known as lattice points, found throughout their entire geometry. Polycrystalline materials are made up of smaller single crystals that are aligned randomly

with respect to one another and amorphous structures have no order in their atomic structure.

Transition metal oxides exhibit a variety of semiconducting properties that can be noticeably tuned by defects in their stoichiometry. Unlike other metals, transition metals have properties that noticeably change based on their d-shell electrons.<sup>2</sup> These semiconducting oxides have phase transitions that, often irreversibly, alter the crystal structure resulting in changes to physical, magnetic, and electrical properties. Conduction in metal oxides can either be electronic or ionic where ionic conduction typically occurs in an aqueous solution such as a battery.

### 2.1.2 Titanium Dioxide

Since the discovery of hydrogen production via photoelectrochemical water splitting,<sup>5-7</sup> TiO<sub>2</sub> films have been one of the most widely studied transition metal oxides for its unique semiconductor properties. TiO<sub>2</sub> crystallizes into three distinct polymorphs where anatase, shown in Figure 2-3, is generally accepted to have higher electronic

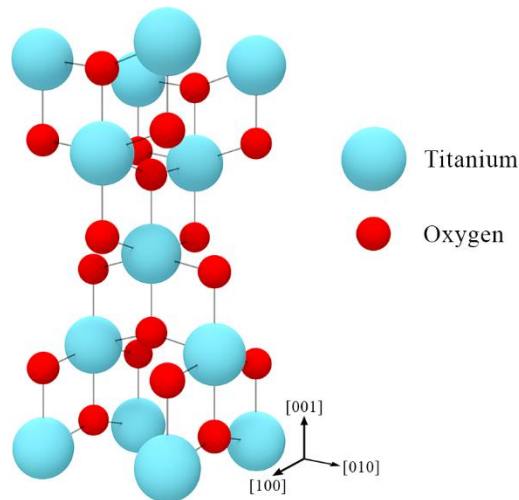


Figure 2-3: Illustration of the anatase crystal structure of TiO<sub>2</sub> with lattice parameters  $a=3.782 \text{ \AA}$  and  $c=9.502 \text{ \AA}$ .

efficiencies in nanostructures compared to its rutile and brookite phases.<sup>8</sup> Rutile and anatase TiO<sub>2</sub> have tetragonal structures with lattice constants  $a=b=4.594 \text{ \AA}$  and  $c=2.96 \text{ \AA}$  for rutile and  $a=b=3.782 \text{ \AA}$  and  $c=9.502 \text{ \AA}$  for anatase. These crystal phases are considered to have wide bandgaps where rutile has a direct bandgap energy of 3.0 eV and anatase with an indirect band gap of 3.2 eV as shown in Figure 2-4. Anatase irreversibly transforms into rutile when annealed at temperatures above 550°C. It is important to note that TiO<sub>2</sub> is an n-type semiconductor material, thus the position of the fermi energy lies below the conduction band.

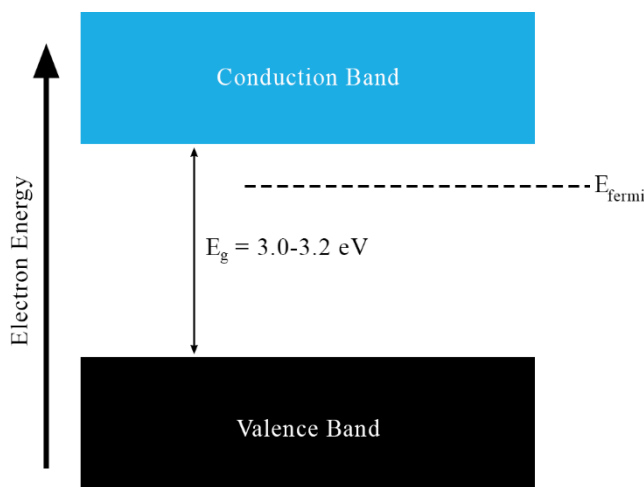


Figure 2-4: Band diagram of TiO<sub>2</sub>.

Nanostructures such as TiO<sub>2</sub> nanotubes (NTs) have gained a considerable amount of scientific interest due to their high specific surface area, tunable geometries, and favorable electrical properties. It is often used in a variety of applications such as batteries,<sup>9-12</sup> electrocatalysis,<sup>13,14</sup> filtration systems,<sup>15,16</sup> gas sensors,<sup>17-21</sup> hydrogen production and storage,<sup>22-27</sup> photovoltaic cells,<sup>7,28-31</sup> and, recently, memristors.<sup>32-37</sup> Although there are many techniques to prepare TiO<sub>2</sub>-NTs, such as sol gel and template assisted methods, electrochemical anodization offers a high control over the pore diameter, interpore

distance, wall thickness, as well as the regularity and defect ratios.<sup>38-47</sup> Recent studies, for example, have analyzed the effects of  $\text{NH}_4\text{F}$  and water concentrations in an ethylene glycol electrolyte and reported on the optimum conditions to grow self-organized, hexagonally arranged NTs with a low defect ratio.<sup>48-50</sup>

Nonstoichiometric  $\text{TiO}_2$  provides further improvements in electronic conductivity and can be achieved through the partial removal of oxygen ions.<sup>51,52,61,62,53-60</sup> These oxygen vacancies ( $\text{V}_\text{o}$ ) have been reported to increase the photocatalytic activity of  $\text{TiO}_2$  through the formation of  $\text{Ti}^{3+}$  ions and the electrons left behind from oxygen ions. The energy level for donor states due to the  $\text{V}_\text{o}$  is located between 0.75 and 1.18 eV below the conduction band and have an even narrower optical gap width.<sup>59,63</sup> The distribution of  $\text{V}_\text{o}$  is currently unknown and found to be stable at subsurface levels. Surface  $\text{V}_\text{o}$  directly assist in aqueous applications such as water dissociation and oxygen adsorption.<sup>64</sup> Figure 2-5 illustrates the possible configuration of  $\text{V}_\text{o}$  sites in an anatase  $\text{TiO}_2$  supercell (space group:  $I4_1/amd$ ). Using

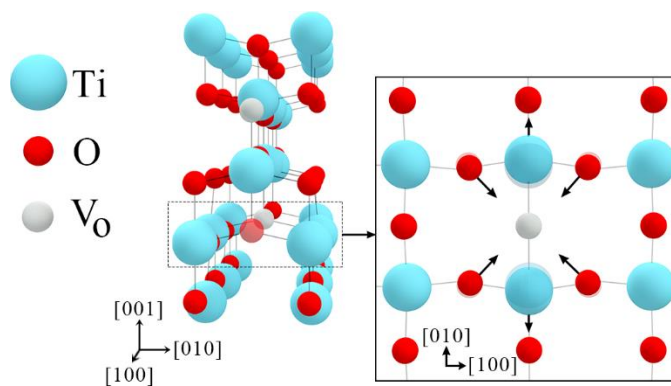


Figure 2-5: Illustration of oxygen vacancies in an anatase  $\text{TiO}_2$  supercell.

computational DFT models, others have shown neighboring O atoms radially move toward the  $\text{V}_\text{o}$  and Ti atoms are relaxed in an outward direction.<sup>65</sup>

## 2.2 Metal-Semiconductor Contacts

Metal-Semiconductor (M-S) contacts are an important aspect to the fabrication of electronic devices. There are essentially two types of M-S contacts: rectifying and ohmic. Ferdinand Braun was the first to document a rectifying behavior in 1874 Germany using lead sulfide on a thin wire.<sup>66</sup> For over a century, this unidirectional current behavior has been investigated for a number of semiconductor materials and nanostructures.

In rectifying M-S contacts, or Schottky junctions, the metal work function ( $\phi_m$ ) relative to the semiconductor material, is considered. As a metal makes contact with a semiconductor, their Fermi energy levels align, resulting in the semiconductor energy bands to bend either up or down forming a barrier expressed by Schottky and Mott as

$$\phi_{sb} = \phi_m - \chi \quad (2.6)$$

where  $\phi_{sb}$  and  $\chi$  are denoted as the barrier height and the electron affinity, respectively.<sup>67,68</sup>

In an n-type semiconductor,  $\phi_m$  will need to have an energy greater than  $\chi$  to form a barrier height ( $\phi_{sb}$ ) as shown in Figure 2-6(a,c).

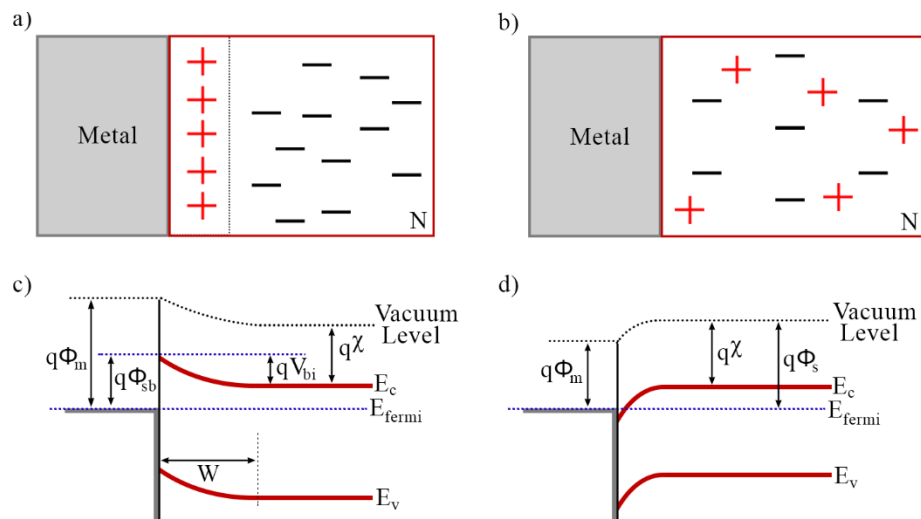


Figure 2-6: Illustration of (a) a Schottky and (b) ohmic contact with an n-type semiconductor and their (c-d) corresponding electron energy band diagrams at thermal equilibrium.



The contact exhibits an ohmic behavior in an n-type semiconductor, Figure 2-6(b,d), when  $\phi_m$  is less than  $\chi$ . Ohmic contacts produce no barrier due to the lack of potential difference in surface charges of both materials. This M-S mechanism allows electrons to flow in either direction. Work function values for common metal contacts are provided in Table 2-1 given in electron volts (eV).

Table 2-1: Metal work functions for common semiconductor contacts.

<b>Metal</b>	<b><math>\phi_m</math> (eV)</b>
Al	4.28
Au	5.1
Pt	5.65
Ti	4.33

The net current diffusion flux in the M-S interface is characterized using the probability distribution of electrons leaving the surface of hot metals and semiconductor materials. This thermionic emission mechanism is applied to determine current density through the interface using the assumption that the flux through a semiconductor surface is continuous into the metal given as Equation (2.7).<sup>69</sup>

$$J = J_s = J_m$$

$$J = J_s - J_m \quad (2.7)$$

The works of Schottky et al. have led to an idealized current-voltage (J-V) relation following thermionic emission theory and is expressed by

$$J = J_0 \left[ \exp\left(\frac{qE_a}{\eta k_B T}\right) - 1 \right] \quad (2.8)$$

where  $\eta$  is a dimensionless ideality factor.  $J_0$  is the reverse saturation current which can be expressed in three-dimensions as

$$J_0 = \frac{4q\pi m^* k_B^2}{h^3} \cdot T^2 \cdot \exp\left(-\phi_{sb}/k_B T\right) \quad (2.9)$$

and in 2D as

$$J_{0,2D} = \frac{q\sqrt{8\pi m^* k_B^3}}{h^2} \cdot \sqrt{T^3} \cdot \exp\left(-\phi_{sb}/k_B T\right) \quad (2.10)$$

where the derivation is provided in appendix I. The first term is known as the Richardson constant denoted as  $A^*$  with units of  $[A/cm^2 K^2]$ . The J-V characteristic of a Schottky diode, shown in Figure 2-7, presents the ideal case where  $\eta = 1$ . The extraction of electrical properties such as the Schottky barrier height and  $\eta$  will be detailed in the next Chapter.

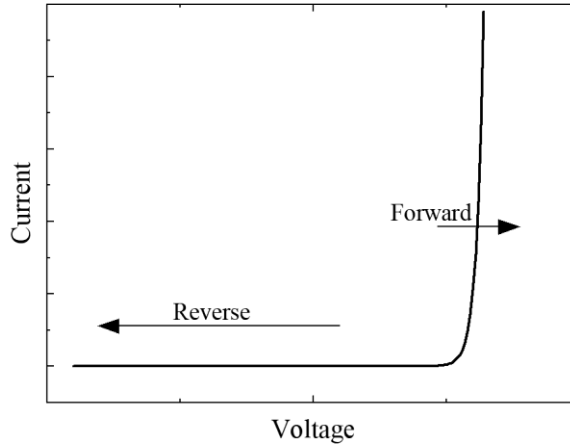


Figure 2-7: Ideal diode J-V characteristics where the ideality factor  $\eta=1$ .

An illustration of the current density mechanism is provided in Figure 2-8 where a space charge region, or depletion region, is formed between the metal and semiconductor. When the diode is forward biased, the depleted region is small enough to allow electrons to hop over the barrier and into the metal. Alternatively, during reverse bias conditions, a buildup of minority charges fill the semiconductor widening the depletion region and preventing electrons from flowing into the semiconductor from the metal.

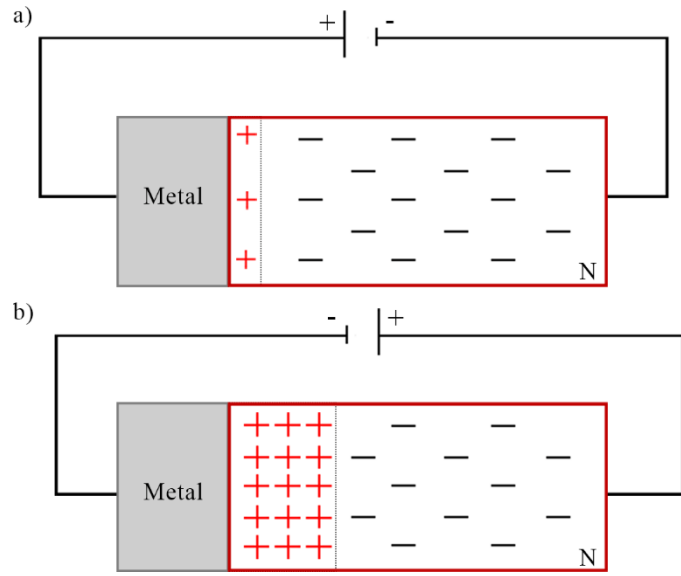


Figure 2-8: Illustration of the (a) forward and (b) reverse bias mechanism for a rectifying metal contact on n-type semiconductors.

## 3 METHODS

### 3.1 Fabrication

The fabrication of a Schottky diode requires depositing a metal onto the surface of the semiconductor to form an M-S interface. The goal is to create a conformal Pt layer throughout an ordered array of TiO<sub>2</sub>-NTs as illustrated in Figure 3-1. This section reviews the fabrication steps taken for this study.

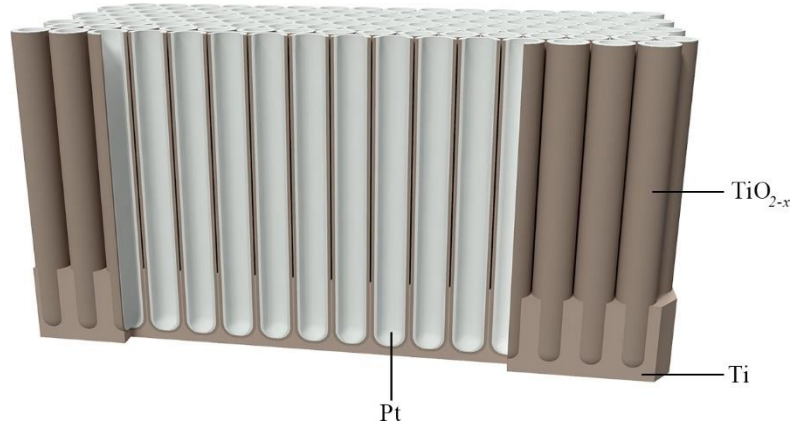


Figure 3-1: Design of a conformal TiO<sub>2</sub>-NT Schottky diode.

#### 3.1.1 Electrochemical Anodization

The electrochemical process to develop a uniform array of TiO<sub>2</sub>-NTs requires a unique balance between the concentration of ammonium fluoride (NH<sub>4</sub>F) and water in an ethylene glycol solution. The quantities for this electrolyte solution are based on the initial amount of NH<sub>4</sub>F measured and given by equations (3.1) and (3.2).

$$V_{ethylene\ glycol} = \frac{m_{NH_4F}}{wt\%_{NH_4F}} * \frac{1 - wt\%_{NH_4F} - vol\%_{H_2O}}{\rho_{ethylene\ glycol}} [mL] \quad (3.1)$$

$$V_{H_2O} = (V_{ethylene\ glycol} + 0.991m_{NH_4F}) \cdot \frac{vol\%_{H_2O}}{1 - vol\%_{H_2O}} [mL] \quad (3.2)$$

Table 3-1 and Table 3-2 show the scalar quantities needed for the volume of ethylene glycol and water, respectively, for a given combination of NH<sub>4</sub>F and water concentrations.

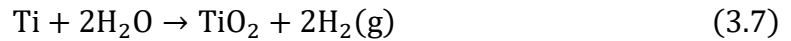
Table 3-1: Scalar quantities for the volume of ethylene glycol (mL) needed for a given wt% NH<sub>4</sub>F and vol% water.

<b>NH<sub>4</sub>F\H<sub>2</sub>O</b>	<b>3.0%</b>	<b>4.0%</b>	<b>5.0%</b>	<b>6.0%</b>	<b>7.0%</b>	<b>8.0%</b>	<b>9.0%</b>	<b>10.0%</b>
<b>0.1%</b>	870.5	861.5	852.5	843.5	834.5	825.5	816.6	807.6
<b>0.2%</b>	434.8	430.3	425.8	421.3	416.8	412.3	407.8	403.3
<b>0.3%</b>	289.6	286.6	283.6	280.6	277.6	274.6	271.6	268.6
<b>0.4%</b>	216.9	214.7	212.5	210.2	208	205.7	203.5	201.2

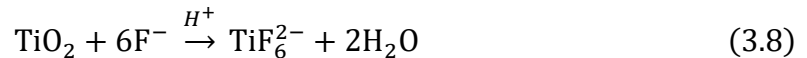
Table 3-2: Scalar quantities for the volume of deionized water (mL) needed for a given wt% NH<sub>4</sub>F and vol% water.

<b>NH<sub>4</sub>F\H<sub>2</sub>O</b>	<b>3.0%</b>	<b>4.0%</b>	<b>5.0%</b>	<b>6.0%</b>	<b>7.0%</b>	<b>8.0%</b>	<b>9.0%</b>	<b>10.0%</b>
<b>0.1%</b>	9.0	18.0	27.0	35.9	44.9	53.9	62.9	71.9
<b>0.2%</b>	4.5	9.0	13.5	18.0	22.5	27.0	31.4	35.9
<b>0.3%</b>	3.0	6.0	9.0	12.0	15.0	18.0	21.0	24.0
<b>0.4%</b>	2.2	4.5	6.7	9.0	11.2	13.5	15.7	18.0

The oxidation process for Ti is defined through the following balanced reaction equations where hydrogen gas is released as a result.<sup>49</sup>



Under an applied electric field, the fluorine ions interact with the TiO<sub>2</sub> layer closest to the Ti anode surface which creates a porous pattern resulting in the formation of nanotubes. The following balanced equations describe the formation of TiF<sub>6</sub><sup>2-</sup> species.





In this work, a 32  $\mu\text{m}$  thick Ti foil (15 mm x 10 mm) is placed into the electrolyte solution with Pt electrodes placed perpendicular to the Ti surface on both sides as illustrated in Figure 3-2. The concentration of the electrolyte is initially set to 0.5 wt%  $\text{NH}_4\text{F}$  and 2 vol% water then later changed to 0.4 wt%  $\text{NH}_4\text{F}$  and 10 vol% deionized water. A 60 V potential is applied between the Pt cathodes and Ti anode for 1 hour before ultrasonically cleaning the initial porous structure.

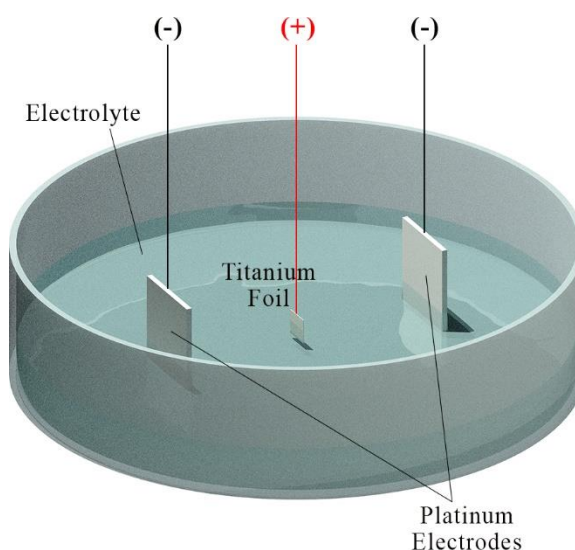


Figure 3-2: Configuration to electrochemically fabricate double sided  $\text{TiO}_2$ -NTs.

A two-step anodization process is implemented where the initial nonuniform surface structure is removed. Illustrated in Figure 3-3, the initial porous structure contains a randomly arranged etching pattern. At the Ti interface, however, is an etched porous pattern that can be used as a starting template for new NTs to form. Therefore, removing the initial porous structure is necessary to ensure a uniform NT growth.

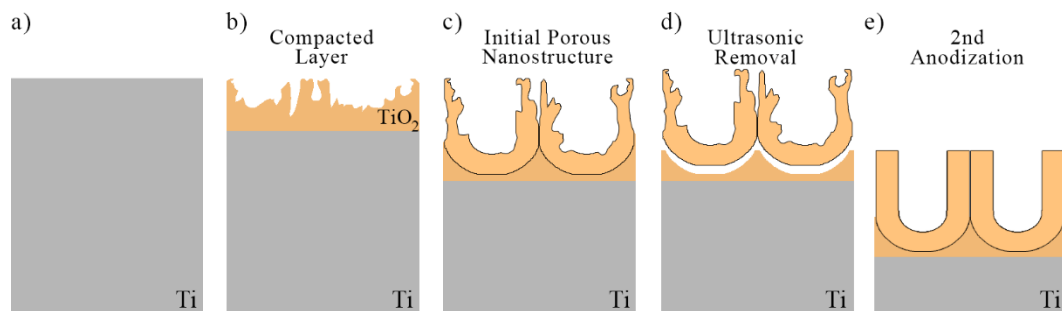


Figure 3-3: Illustration of the two-step anodization process on (a) a thin Ti foil. Initial anodization (b) forms a compacted TiO<sub>2</sub> layer before (c) forming a randomly arranged porous structure. (d) Pores are ultrasonically removed, leaving behind a surface pattern for the (e) second anodization step.

### 3.1.2 Heat Treatment

Once the Ti foils have been anodized, the crystal structure is, by default, amorphous and requires a heat treatment to crystallize the NTs. In this study, the annealing temperature was set to 550°C for two hours with a steady temperature ramping rate of 3°C/min. Annealing was performed under atmospheric conditions, pure O<sub>2</sub>, as well as vacuum pressures. Figure 3-4 is the high temperature furnace used throughout this experiment.

Nonstoichiometric TiO<sub>2</sub> was obtained by re-annealing the samples in a vacuum environment. Initial annealing is used to remove organic materials and to eliminate residual

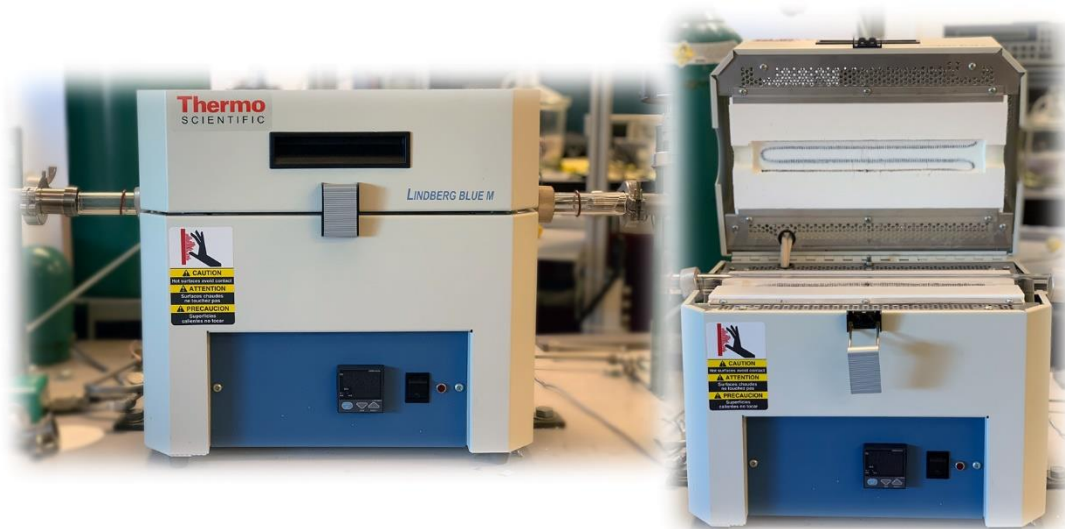


Figure 3-4: Tube furnace for high temperature annealing.

fluorine ions from the lattice structure. After vacuum annealing, the TiO<sub>2</sub>-NTs appear blackened due to the formation of Ti<sup>3+</sup> ions. A post-heat treatment was applied to both stoichiometric and nonstoichiometric samples in atmospheric and vacuum environments, respectively.

### **3.1.3 Sputter Deposition**

Sputter deposition offers the ability to produce a Schottky junction by depositing metals onto a semiconductor material. However, at nanoscale, the resolution of metal deposition is not sufficient.

For this study, sputter deposition will be used to strictly create a sacrificial gold (Au) layer. This sacrificial layer acts as a temporary protective layer to be later removed using a selective Au etchant or aqua regia solution. The sputtering chamber, Figure 3-5, is pumped down to a base pressure of about 7  $\mu$ Torr before flowing argon (Ar) gas at a constant working pressure of 10 mTorr. The gas is then subject to an RF power of 75 W, producing glow discharge given off by the now energetic, ionized gas, or plasma. The plasma gas bombards the 2-inch Au target and releases atoms in random directions where some will land on the Ti foil providing a complete coverage over time.



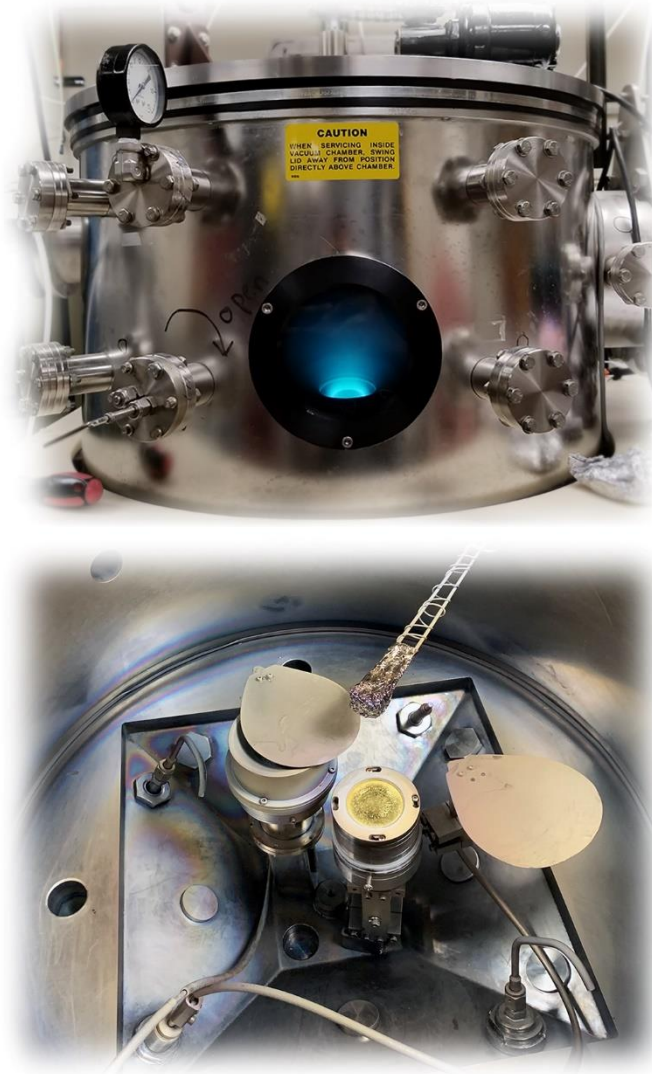


Figure 3-5: RF sputter deposition chamber.

### 3.1.4 Atomic Layer Deposition

Atomic layer deposition (ALD) is a type of chemical vapor deposition where gasses are injected into a chamber to deposit materials onto a surface.<sup>70</sup> The recent developments in atomic layer deposition (ALD) have provided a precise growth control of single-element, ultrathin conformal films on nanostructures.<sup>71</sup> This thesis implements a two-step reaction

sequence where a precursor gas is pumped into the chamber followed by a reactant gas, leaving behind an atomically deposited single-element, Pt.

The precursor gas, trimethyl(methylcyclopentadienyl)platinum(IV), is diffused into the porous TiO<sub>2</sub>-NTs with an exposure time of 45s then purged of any excess gases. O<sub>2</sub> is used as the reactant gas to bind to the organic compound which will leave behind a single platinum particle as illustrated in Figure 3-6, then purged from the system before a new cycle begins.

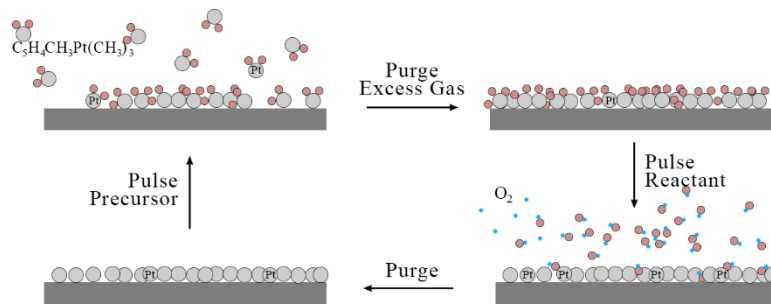


Figure 3-6: Typical ALD process cycle for Pt film growth.

ALD is a self-limiting surface reaction such that the reaction ends when all surface sites have been occupied by the precursor gas. In this regard, it is possible to form a uniform metal-semiconductor interface while making use of the large surface area found in 1D structures. Porous materials create an interesting challenge as the diffusion flux into each pore is dependent on the exposure time and concentration of the available Pt precursor gas.<sup>72-74</sup> There are three modes of deposition throughout a nanotube or trench structure: reaction, diffusion, and recombination limited, illustrated in Figure 3-7.<sup>75</sup> It should be noted that a high concentration of the precursor gas will provide full surface coverage, leading to a reaction-limited condition.

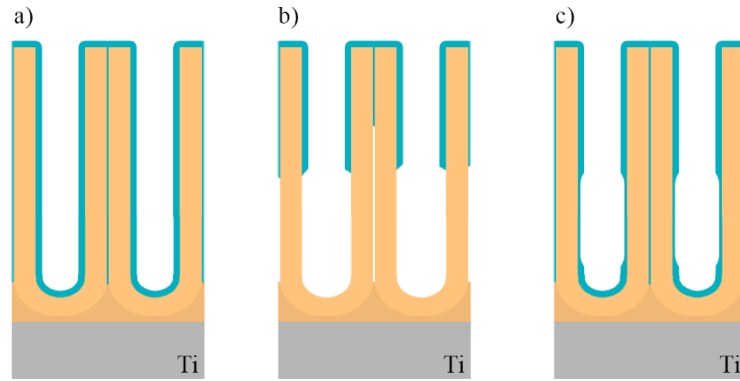


Figure 3-7: The modes of ALD deposition into porous structures where (a) a conformal deposition occurs in a reaction-limited condition, (b) partial surface coverage for diffusion-limited modes, and (c) an uneven deposition rate towards the bottom of the nanostructure in recombination-limited modes.

Since ALD will coat the entire sample, the sacrificial Au layer was used to prevent the device from applying Pt to the anode and cathode of the diode, resulting in an electrical short. Au can be etched using a selective Au etchant such as GE-8148 or Aqua Regia (nitric acid and hydrochloric acid). Figure 3-8 shows the device before and after Pt deposition and Au removal where a clear Pt boundary is visible.

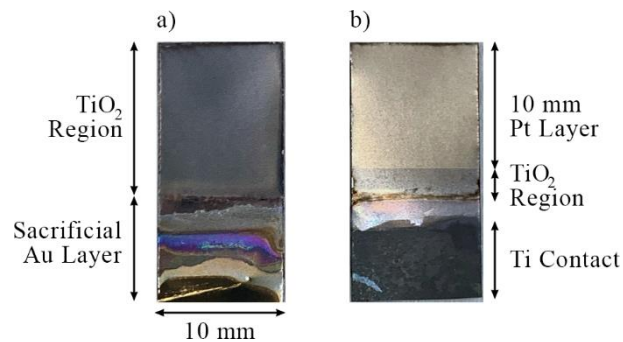


Figure 3-8: (a) Annealed TiO<sub>2</sub> sample with a protective Au layer and (b) after Pt-ALD with the Au layer removed.

During the initial fabrication iterations, a 10-second exposure time was performed. As the NTs became longer and wider, a 45-second exposure time was required to diffuse to the bottom of the pores. Any defects within the nanotubes such as cracks on the surface or

within the NTs created an opening for Pt atoms to reach the Ti foil beneath causing an electric short between the anode and cathode.

## **3.2 Characterization**

### **3.2.1 X-Ray Diffraction**

X-ray diffraction (XRD) is a technique used to analyze the structure of bulk materials by capturing the angles of reflected waves with respect to the incident waves. This is a nondestructive and indirect characterization technique that uses the wavelength ( $\lambda$ ) of x-rays (Cu K- $\alpha$  = 1.54 Å) to penetrate between the interatomic distances of the crystal lattice points.<sup>76</sup> When incident x-rays collide with a crystal lattice point, photons at each crystal plane are reflected away from the surface. These reflected waves can either constructively or destructively interfere with one another resulting in either sharp peaks or noise, respectively, at various incident angles. These peak locations can then be applied to Bragg's law to identify the interatomic spacing ( $a$ ) between each plane and given as

$$2a \cdot \sin \theta = n\lambda \quad (3.10)$$

where  $n$  indicates the reflection order. This technique allows us to gather material information such as the crystal structure, size, and composition.

### **3.2.2 Ultraviolet-Visible Spectroscopy**

Ultraviolet-visible spectroscopy (UV/Vis) was used to examine the absorption of the electromagnetic spectrum in both stoichiometric and nonstoichiometric TiO<sub>2</sub>-NTs. This technique uses ultraviolet and visible light ranges and measures the intensity of light

transmitted through a sample while comparing it to a reference measurement. Nonstoichiometric TiO<sub>2</sub> appears much darker than oxygen rich, stoichiometric TiO<sub>2</sub> samples due to the Ti<sup>3+</sup> species found throughout the lattice points. This study was used to show the difference in absorbance between stoichiometric and nonstoichiometric TiO<sub>2</sub> films.

### **3.2.3 Scanning Electron Microscopy**

Scanning electron microscopy (SEM) and energy-dispersive x-ray spectroscopy (EDX) were used to examine the surface and cross-sectional areas of the TiO<sub>2</sub> nanostructures. SEM systems use an electron beam to eject secondary and backscattered electrons from the material producing a topographical image. Secondary electrons provide information regarding the surface structure such as locating any low-density structures whereas backscattered images provide information regarding the subsurface features such as the density of material. A FEI Quanta 600 FEG Environmental SEM, Figure 3-9, was used for this analysis and paired with ESPRIT and ImageJ software.



Figure 3-9: FEI Quanta 600 FEG Environmental SEM

Parameters such as average diameter, pore circularity ratio, and perimeters were gathered using the ESPIRIT software. The circularity ratio is calculated using the following:

$$\text{circularity ratio} = \frac{4\pi \cdot \text{Area}}{\text{Perimeter}^2} \quad (3.11)$$

The Fast Fourier Transform (FFT) was performed on images using the imageJ software. This provides us with information on the regularity of the porous structure where a hexagonal pattern would indicate a regular periodicity of pore openings. In irregular pore distributions the FFT would appear to be circular.

In addition to imaging, the incident electron beam produces characteristic X-ray photons that carry information regarding the chemical composition of the material. The energy that these photons carry is related to the outer shell electrons filling vacancies in

the inner shell created by the electron beam. As we recall from band theory, electrons require energy to move from the valence band to the conduction band. When electrons move in the opposite direction, energy is lost or emitted via photons. As seen in Figure 3-10, SEM systems can be easily fitted with EDS detectors to capture these photon energies and characterized on an energy spectrum.

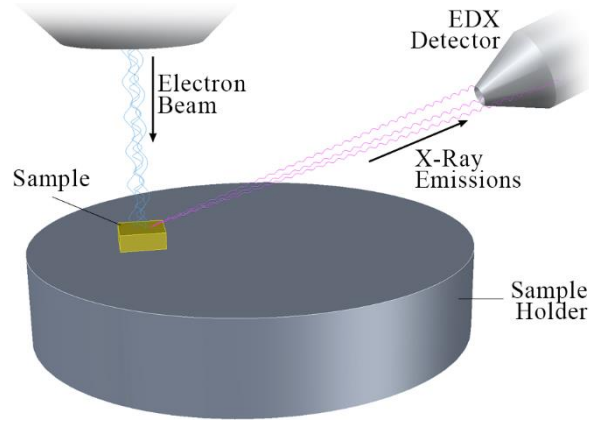


Figure 3-10: Operational overview of an EDS detector.

### 3.2.4 Current-Voltage and Capacitance-Voltage

The Schottky barrier height, ideality factor, and series resistance were extracted from the I-V measurements using thermionic emission theory, Cheung-Cheung's method, as well as Norde's method. The ideality factor is extracted using the log J-V forward bias slope for thermionic emission theory and Norde's method by

$$\eta = \frac{dV}{d \ln J} \frac{q}{k_B T} \quad (3.12)$$

Adjustments in the thermionic emission equation is required to consider the series resistances ( $R_s$ ) in the material. Equation (2.8) changes as follows

$$J = J_0 \left[ \exp \left( \frac{qE_a - JR_s}{\eta k_B T} \right) - 1 \right] \quad (3.13)$$

The Norde method demonstrates a technique to extract the series resistance and Schottky barrier height by applying the following equations to the I-V measurements.

$$F(V) = \frac{V}{\gamma} - \frac{k_B T}{q} \frac{J}{A^* T^2} \quad (3.14)$$

$$\phi_{sb} = F(V_{\min}) + \frac{V_{\min}}{\gamma} - \frac{k_B T}{q} \quad (3.15)$$

$$R_s = \frac{k_B T}{q} \frac{\gamma - \eta}{J(V_{\min})} \quad (3.16)$$

The term  $\gamma$  is the next integer greater than  $\eta$  and  $V_{\min}$  refers to minimum forward biased value in Norde's function,  $F(V)$ .<sup>77</sup>

Cheung and Cheung later proposed an alternative method to find the ideality factor, series resistances, and Schottky barrier height. The Cheung and Cheung functions,  $H(J)$ , are stated as follows:

$$\frac{dV}{d \ln J} = IR_s + \eta \frac{k_B T}{q} \quad (3.17)$$

$$H(J) = V - \eta \frac{k_B T}{q} \ln \left( \frac{J}{A^* T^2} \right) \quad (3.18)$$

$$H(J) = IR_s + \eta \phi_{sb} \quad (3.19)$$

A linear approximation is required to determine the intercept of the y-axis in Equation (3.16) and (3.18) as  $I$  approaches zero.<sup>78</sup> The y-intercept provides both  $\eta$  and  $\phi_{sb}$  with slope  $R_s$ .



The capacitance-voltage measurements were captured for stoichiometric and nonstoichiometric TiO<sub>2</sub> diodes; however, parasitic capacitance values are to be expected in a conformal Schottky barrier that will result in deviations from typical characteristic equations. Limitations in the measurement system also prevents using lower testing frequencies to account for nanostructured and memristive materials.

Current-capacitance-voltage measurements are taken using a Keithley 2601A source meter (Figure 3-11a) and a HP 4279 C-V meter (Figure 3-11b) using Au-tipped micromanipulator probes. The current density was measured between -1.5 and 1.5 V for stoichiometric and nonstoichiometric TiO<sub>2</sub> diodes and again post-thermal treatment, while capacitance measurements were taken between -3 and 0 V with an oscillating frequency of 1MHz. Capacitance measurements can be used to determine a number of factors such as the donor concentration ( $N_d$ ) and the barrier height given by

$$C = A \sqrt{\frac{\epsilon_r \epsilon_0 q N_d}{2 \left( V_{bi} + V_R - \frac{k_B T}{q} \right)}} \quad (3.20)$$

where  $A$ ,  $\epsilon_r$ ,  $\epsilon_0$ , and  $V_R$  are the cross-sectional area, permittivity of the semiconductor, relativity of free space, and the applied reverse bias potential.<sup>69</sup> The C-V measurement is typically more accurate in finding the built-in voltage and is found using a linear approximation of the  $1/C^2$  plot and determining the location at which the line crosses the voltage axis.

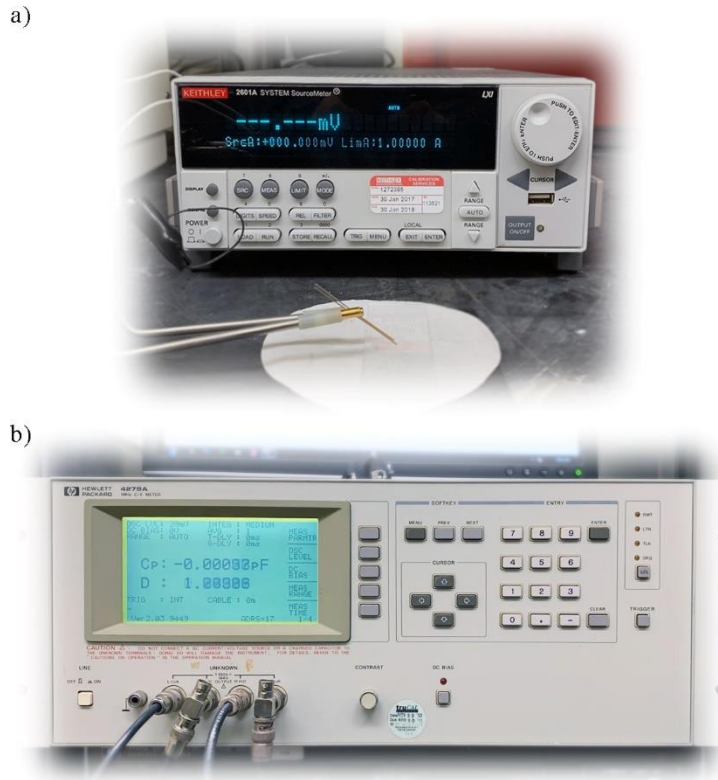


Figure 3-11: (a) Keithley 2601A Source Meter for Current-Voltage measurements and (b) an HP 4279 C-V meter for Capacitance-Voltage measurements.

### 3.2.5 Numerical Methods

The method of linear least-squares approximation is used to find a “best fit” linear approximation to a non-linear set of data points. This numerical technique allows us to solve for the slope of the log J-V plot and the previously mentioned Cheung-Cheung’s functions. This algorithm uses existing data points to determine the coefficients  $a_0$  and  $a_1$  in the following set of equations.<sup>79</sup>

$$y = a_1 \cdot x + a_0 \quad (3.21)$$

$$a_1 = \frac{n(\sum_{i=1}^n x_i y_i) - (\sum_{i=1}^n x_i)(\sum_{i=1}^n y_i)}{n(\sum_{i=1}^n x_i^2) - (\sum_{i=1}^n x_i)^2} \quad (3.22)$$

$$a_0 = \frac{(\sum_{i=1}^n x_i^2)(\sum_{i=1}^n y_i) - (\sum_{i=1}^n x_i)(\sum_{i=1}^n x_i y_i)}{n(\sum_{i=1}^n x_i^2) - (\sum_{i=1}^n x_i)^2} \quad (3.23)$$

The variable  $n$  is defined as the total number of measurement points used to find the linear approximation. The algorithm used is supplied in Appendix II.

## 4 RESULTS

### 4.1 Crystal Structure Analysis using XRD

The TiO<sub>2</sub>-NTs were annealed at 450°C, 550°C, and 750°C to determine the temperature at which crystal phases irreversibly transition from anatase to rutile. Figure 4-1 shows that the anatase crystal structure is present between 450 and 550°C and begin to

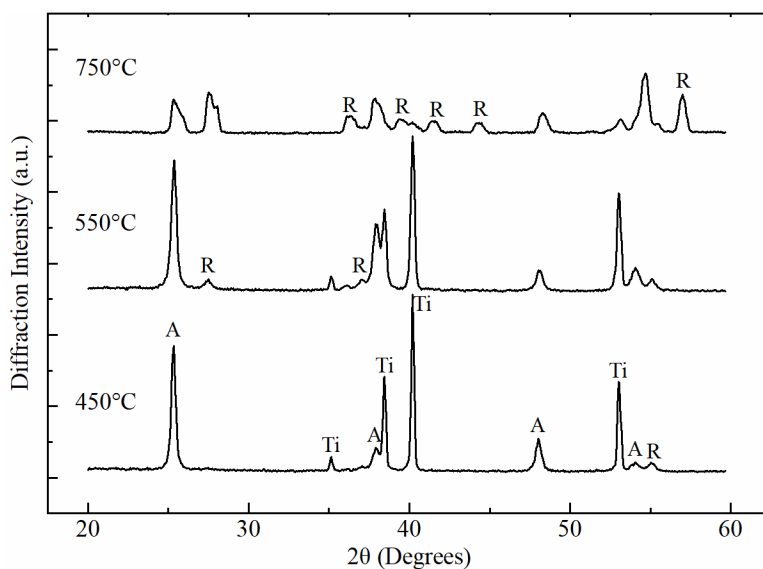


Figure 4-1: X-ray diffraction patterns of TiO<sub>2</sub>-NTs annealed at 450°C, 550°C, and 750°C.

vanish when annealed at higher temperatures. A hexagonally close packed (hcp) Ti crystal structure is present when annealed at or under 550°C and is only found when using an ordered array of NTs. In Figure 4-2, an XRD comparison is made between a Ti foil, nonstructured TiO<sub>2</sub>, and TiO<sub>2</sub>-NTs both annealed at 550°C.

Diffraction angles for anatase TiO<sub>2</sub> were measured at 25.35°, 37.90°, and 48.05°. The initial diffraction angles for rutile peaks were determined to be 27.50°, 36.95°, and 55°; and hcp-Ti at 35.15°.

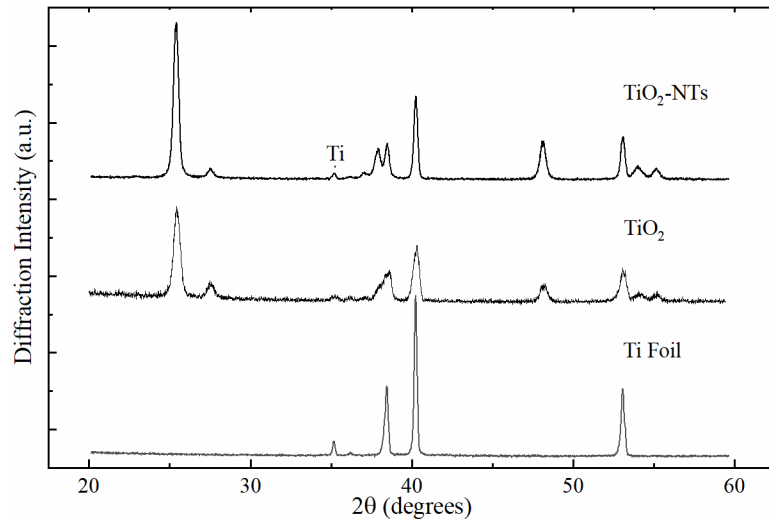


Figure 4-2: X-ray diffraction patterns of a Ti foil, TiO<sub>2</sub> film, and TiO<sub>2</sub>-NTs annealed at 550°C.

## 4.2 Surface and Cross-Sectional Analysis using SEM

The initial anodization parameters involved a 0.5 wt% NH<sub>4</sub>F and 2.0 vol% water concentration. An anodization time of 20 minutes resulted in a topological collapse in tube structure as shown in Figure 4-3. Thermal treatment of these collapsed tubes show randomized nanoparticle features throughout the surface.

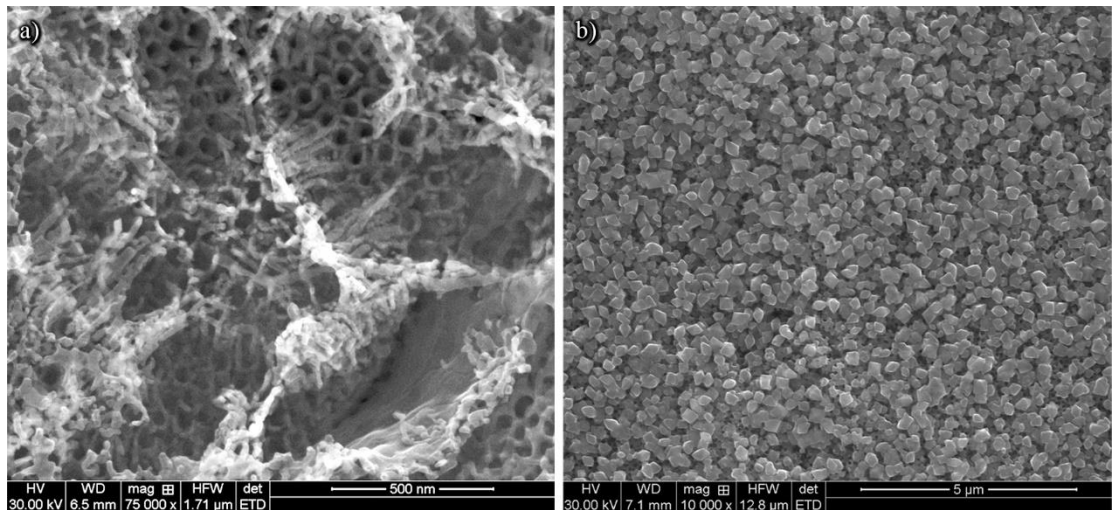


Figure 4-3: Initial anodization trial where the surface of the NTs exhibited (a) a collapse in the porous structure and (b) developed random particle features after thermal annealing.

The backscatter electron image of Figure 4-3a shows a subsurface (approx. 10 nm) formation of nanotubes given in Figure 4-4.

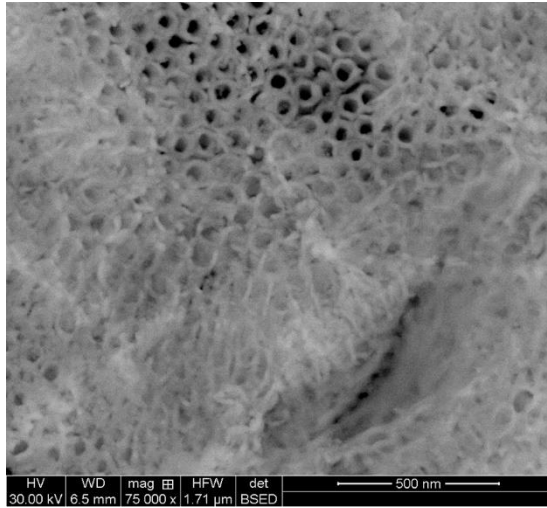


Figure 4-4: Backscatter image of the initial anodization parameters.

In the next iteration the anodization time was reduced to 15 and 10 minutes and revealed a visible porous structure. The surface quality still contained unwanted  $\text{TiO}_2$  crystal features as shown in Figure 4-5.

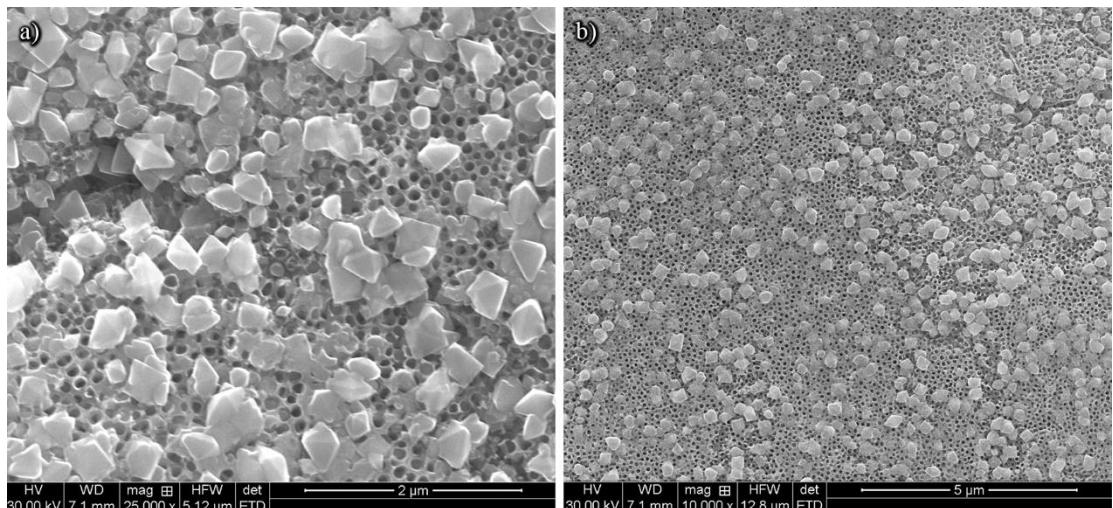


Figure 4-5: 15-minute anodization time where (a) pores are clearly visible but (b) a large-scale distribution of unwanted nanoscale features remained on the surface.

At a 10-minute anodization time, the surface features went away, however, produced a randomly arranged porous structure with deep surface cracks throughout the surface, shown in Figure 4-6. These cracks were found in previous iterations that were not addressed until this iteration.

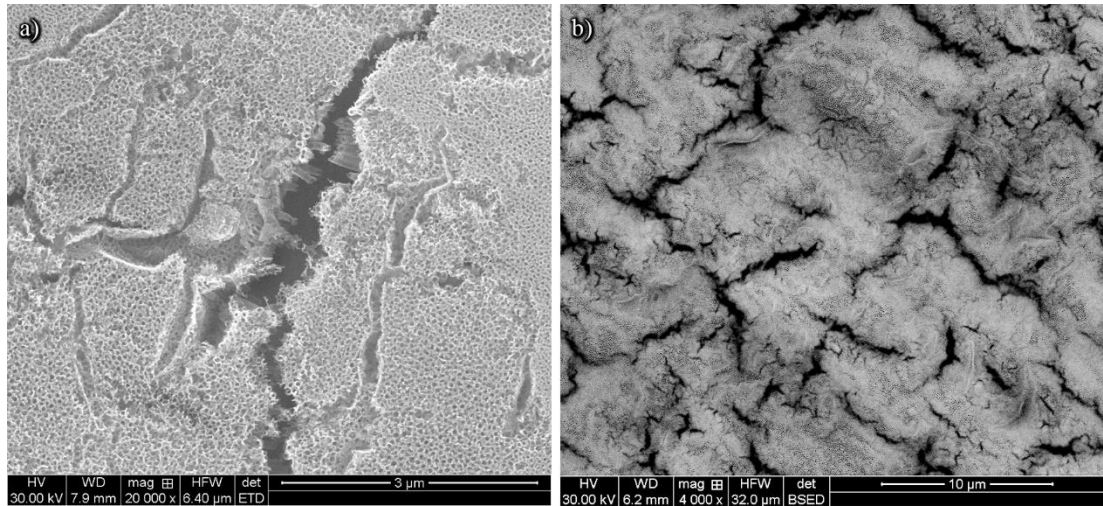


Figure 4-6: (a) 10-minute anodization where surface features are removed, however, (b) subsurface cracks are found throughout the structure using backscatter imaging.

Environmental parameters were found to affect the surface crack propagation such as annealing in atmospheric conditions, pure O<sub>2</sub>, and under vacuum. Vacuum conditions eliminated most surface defects; however, I-V measurements revealed an altered material characteristic when forming a Schottky barrier. The annealing temperature ramping rate was adjusted to 3°C/min for the remainder of this study.

After reducing the anodization time to 3 minutes, the surface structure formed an improved and lowered defect quality under controlled annealing parameters. After Pt deposition, however, the pore openings appeared to dramatically shrink in size, as seen in Figure 4-7a. A cross-sectional backscattered image, Figure 4-7b, shows a dense, brighter portion within the NTs, indicating the locations of Pt-ALD deposition. This deposition

quality will be further discussed in the next section. By reducing the ramping rate and anodization time, the surface defects appeared to be significantly reduced, however, later we find that a change in fluorine ions and water concentration within the electrolyte solution results in the elimination of surface defects.

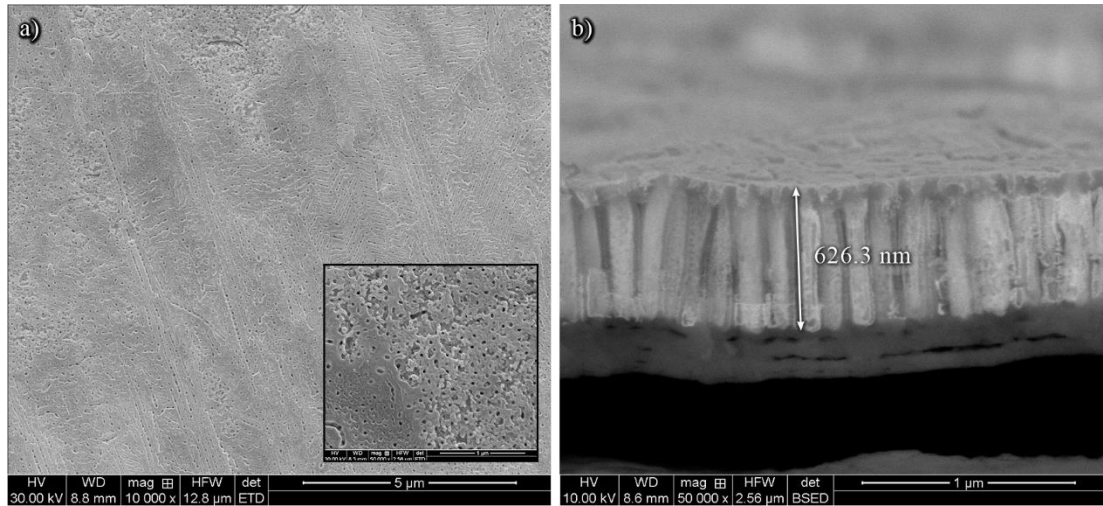


Figure 4-7: (a) 3-minute anodization with an annealing temperature ramping rate of 3°C/min along with the (b) cross-sectional area with NT length of about 625 nm.

A two-step anodization process was examined to eliminate the initial porous film and make use of the surface template to create a more uniform porous structure. The initial nanotubes require a minimum length of about 1 μm to successfully remove them from the Ti film. The sample was submerged in a glass beaker filled with deionized water and ultrasonicated for 1 hr. We can clearly see a crack-free, porous structure after this iteration, however, there is a widely uneven distribution of diameters that range from 60 to 160 nm, as seen in Figure 4-8.



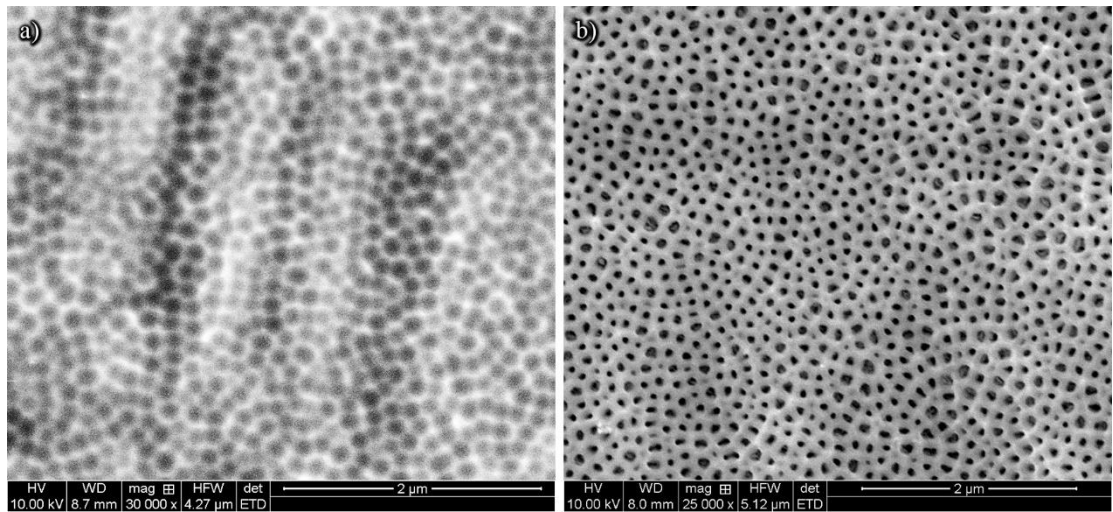


Figure 4-8: (a) Surface pattern left behind after a 1-hour ultrasonic cleaning and the (b) Pt coated porous TiO<sub>2</sub> structure formed after a 2<sup>nd</sup> anodization step.

After reviewing the anodizing solution, adjustments were made such that the wt% NH<sub>4</sub>F and vol% water was changed to 0.4% and 10.0%, respectively. This change allowed for a longer anodization time and resulted in a uniform distribution of pores throughout the surface. Figure 4-9 shows the resulting NT array with its respective FFT. The FFT, using the imageJ software, shows a hexagonal structure indicating that the pores have periodicity and are mostly hexagonally arranged.

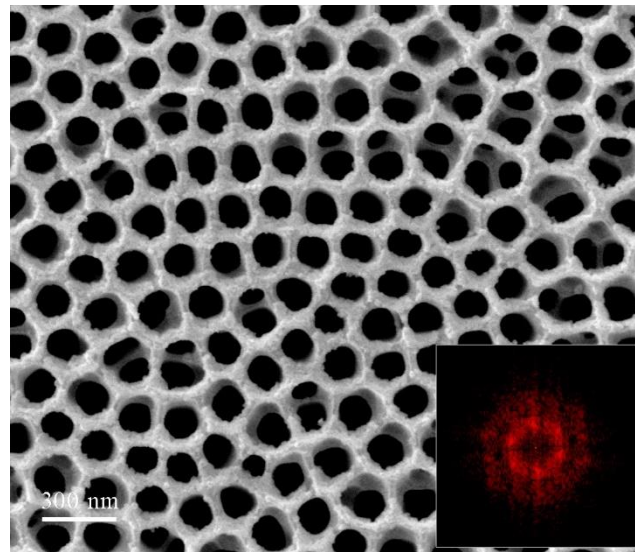


Figure 4-9: SEM image of the Pt/TiO<sub>2</sub> surface with a corresponding Fast Fourier Transform.

The average pore diameter is given in Figure 4-10 where over 60% of the pores, after Pt deposition displayed a pore diameter above 120 nm with an average diameter of 121 nm. Figure 4-11 presents the average circularity and perimeter and was determined to be 1.46 and 372 nm, respectively.

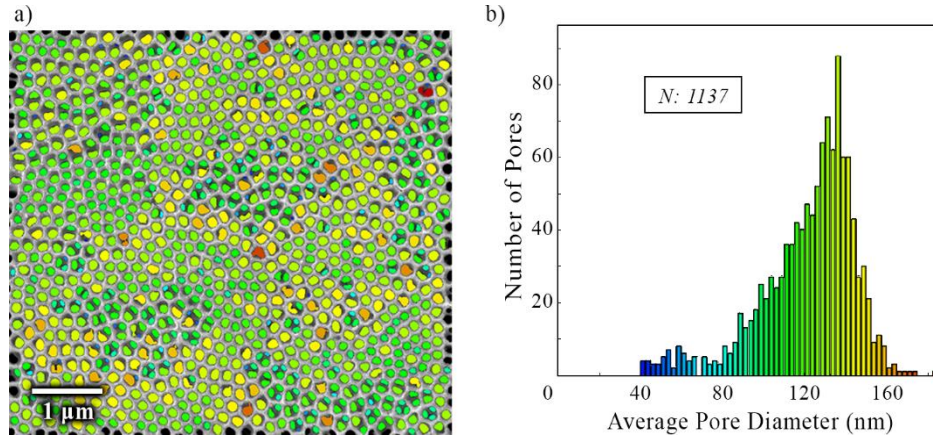


Figure 4-10: Average pore diameter analysis.

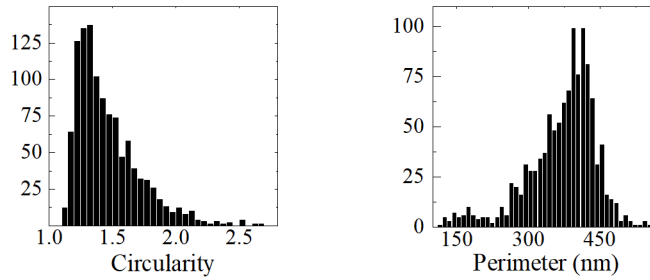


Figure 4-11: Circularity ratio and average pore perimeter.

These values can be used to determine the total surface area of the diode and leads to the values found in the table below.

Table 4-1: Calculated cylindrical surface area, the number of pores per area, and the overall aspect ratio.

Cylindrical Surface Area	Pores per Area	Aspect Ratio = $\frac{\text{length}}{\text{diameter}}$
$1.5 \mu\text{m}^2/\text{pore}$	$30 \text{ pores}/\mu\text{m}^2$	33-35

The growth rate for a given anodization time is characterized by using the cross-sectional images of the NT arrays, presented in Figure 4-12.

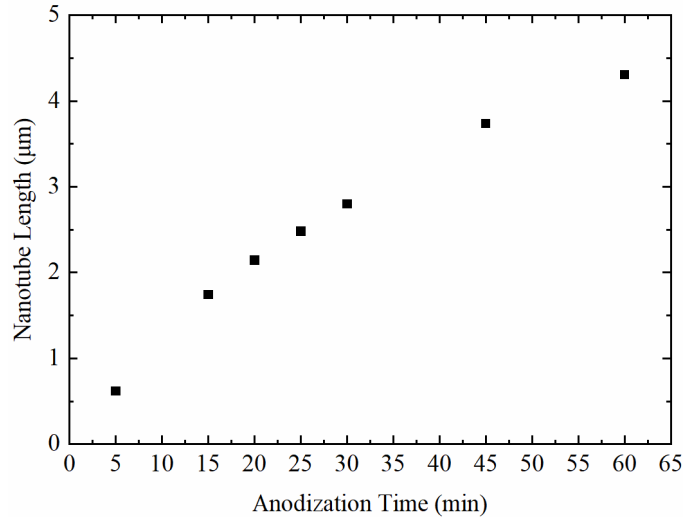


Figure 4-12: NT growth rate vs. Anodization time

### 4.3 Elemental Composition using EDX and Backscatter Imaging

Initial ALD deposition for the short 625 nm NTs resulted in a uniform coverage throughout the porous structure. A 10-second Pt exposure provided enough time to allow the Pt precursor gas to diffuse into the porous structure, as shown in Figure 4-13. Here, an elemental composition is combined to show the location of energetic photons with energies corresponding to the elements Pt, Ti, and O.

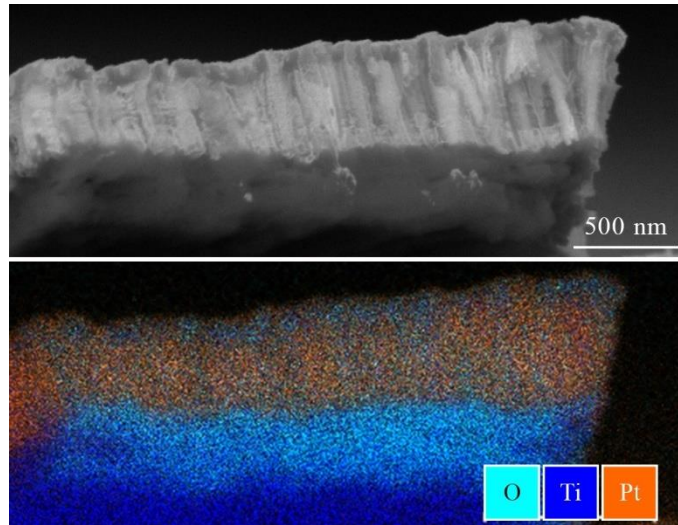


Figure 4-13: EDX analysis of the cross-sectional area of a 625 nm long NT.

Backscattered electron images provide density information where the Pt metal is a higher density than  $\text{TiO}_2$  and shown as a brighter surface. This allows us to visualize the location of Pt deposits throughout the NT structure, as presented in Figure 4-14. These NTs were grown for 45 minutes with a length of  $3.3 \mu\text{m}$  and ALD exposure time of 20 seconds. We can see a high density of metal deposits throughout the inner walls of the NT arrays; however, the exposure time or concentration of the precursor gas will need to be increased to provide a reaction-limited condition.

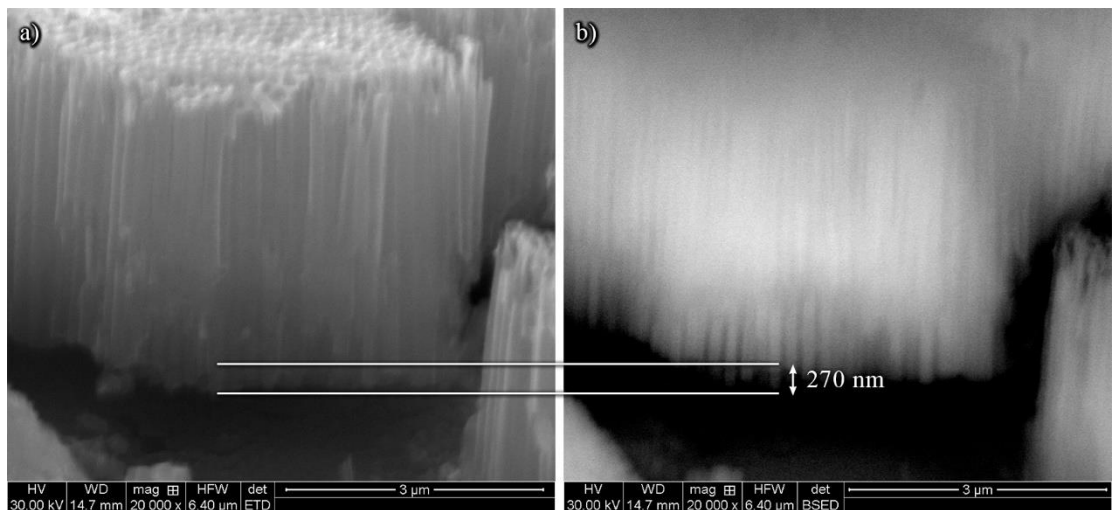


Figure 4-14: (a) Secondary and (b) backscatter electron images showing low density areas indicating a diffusion-limited deposition regime.

The bottom of the NT array indicates a slight Pt discontinuity throughout the inner tube walls as indicated by the horizontal stripes in Figure 4-15. This is likely attributed to the nucleation step in the ALD process where islands are initially formed.<sup>80</sup>

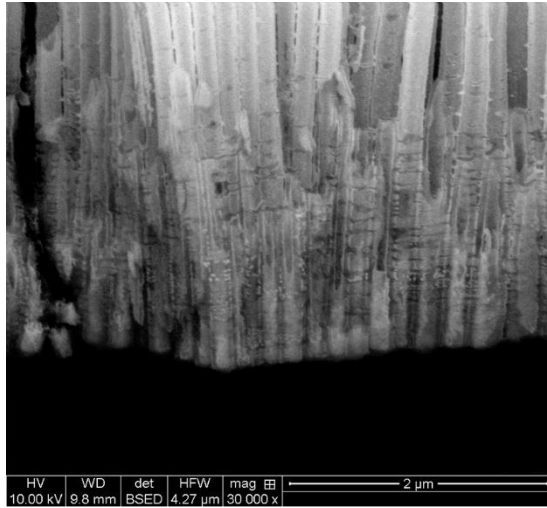


Figure 4-15: Discontinuous Pt deposition at the bottom of the NTs.

NTs were grown for 60-minutes and exposed to the Pt precursor for 45-seconds to ensure conformal deposition. Figure 4-16 shows the EDX analysis of the materials found throughout the Pt/TiO<sub>2</sub>-NT diode.

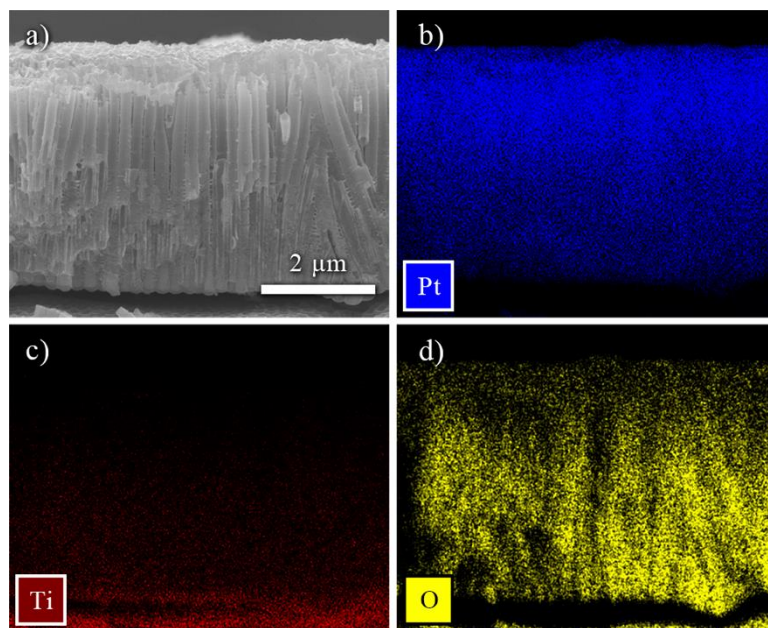


Figure 4-16: The (a) cross section of the Pt/TiO<sub>2</sub>-NT array with a (b-d) corresponding elemental composition map for Pt, Ti, and O.

A brief material comparison was made between samples annealed under atmospheric conditions, pure O<sub>2</sub>, and under vacuum and is presented in Table 4-2.

Table 4-2: Mass % of elements found under different annealing conditions.

Element	Atomic Number	Mass %		
		Atm	O <sub>2</sub>	Vacuum
<b>Titanium</b>	22	61.2	60.5	60.9
<b>Oxygen</b>	8	37.8	38.3	37.8
<b>Fluorine</b>	9	0.0	0.2	0.3

It is important to note that an initial atmospheric annealing is required to remove any residual fluorine ions from the TiO<sub>2</sub> material. The conduction mechanism behind fluorine ions is not yet fully understood for anatase crystal structures, however, these ions will likely lead to a reduction in the bandgap energy due to the modifications of energy levels around the conduction band edge.

## 4.4 UV-Vis Spectrum

Stoichiometric and nonstoichiometric  $\text{TiO}_2$  was obtained through air and vacuum annealing, respectively. Nonstoichiometric samples displayed a darker film due to the  $\text{Ti}^{3+}$  species introduced through oxygen vacancies. The UV-vis analysis shows that in the visible region of the electromagnetic spectrum, nonstoichiometric samples absorbed more photons above 350 nm as shown in Figure 4-17. In the UV region, both samples showed similar absorption ratings where nonstoichiometric  $\text{TiO}_2$  was found to be absorb photons across the entire visible spectrum. These results align with previous literature comparing the two films allowing us to confirm nonstoichiometric  $\text{TiO}_2$ .<sup>81</sup>

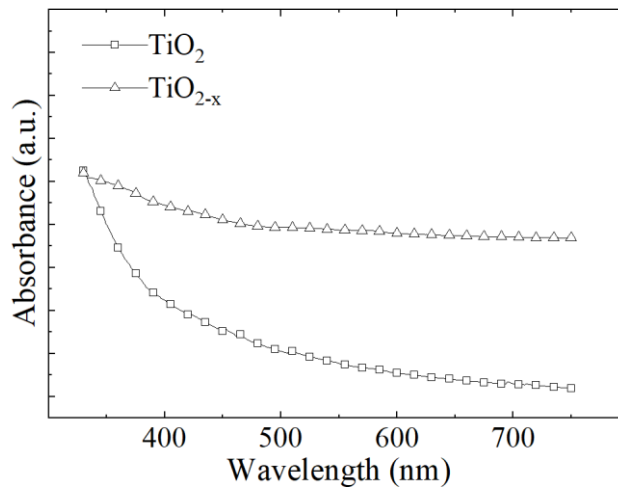


Figure 4-17: UV-vis spectrum of stoichiometric and nonstoichiometric  $\text{TiO}_2$ -NTs.

## 4.5 Current – Voltage Characteristics

Before reviewing the Schottky diode characteristics, it was found that the electrochemical anodization process has a dynamic resistivity as a function of time. Initially, the resistance is nearly zero and then begins to significantly increase over a short period of time, as seen in Figure 4-18.

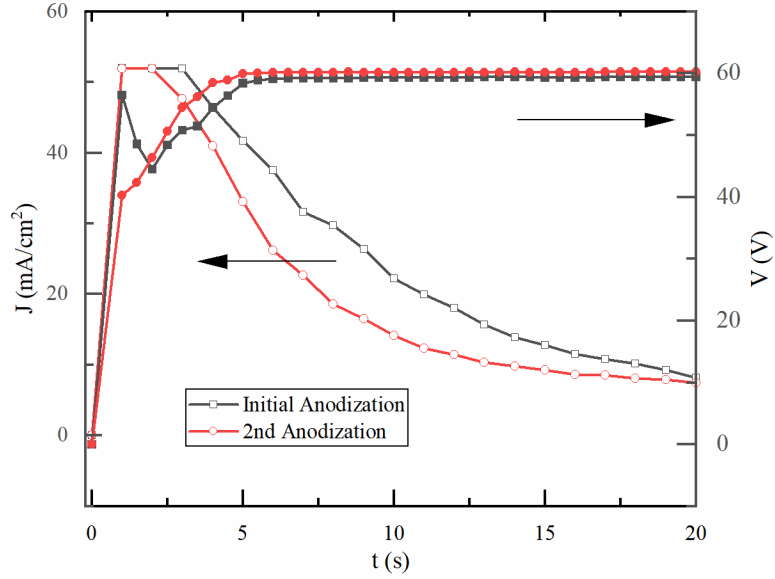


Figure 4-18: Resistance in the electrolyte increases during the anodization process for one minute before slowly decreasing at  $3.3 \text{ m}\Omega/\text{min}$  as Ti ions enter the solution.

Stoichiometric  $\text{TiO}_2$  is plotted in Figure 4-19 where the as-deposited Pt samples were found to have an ideality factor of about 3.7 and the post-thermally treated samples at  $\eta=2.04$ . The semi-log plot of the post-thermal samples is discontinuous due to system limitations in the 2601 source meter.

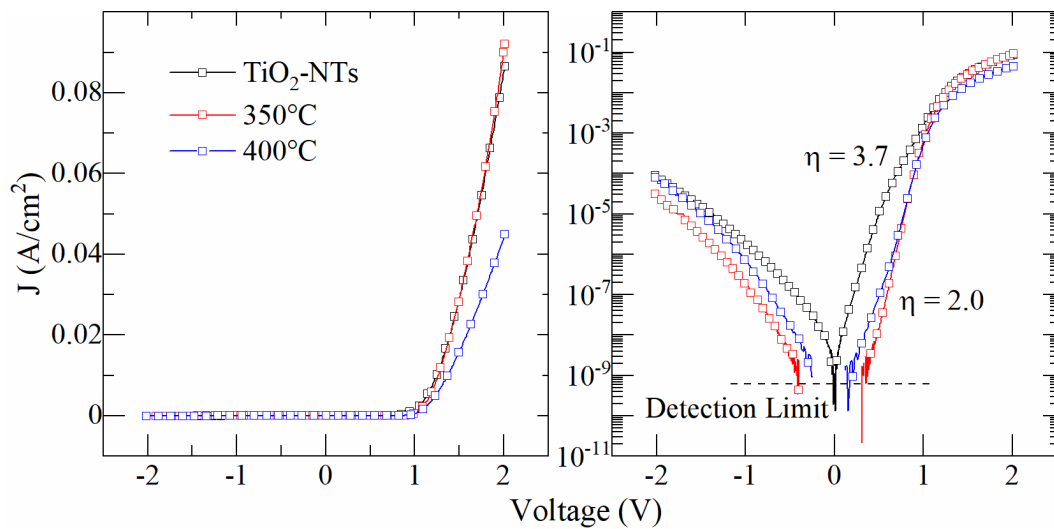


Figure 4-19: (a) Current-Voltage characteristics of stoichiometric  $\text{TiO}_2$ -NT Schottky diodes for the as-deposited Pt and thermally treated diodes. (b) Semi-log plot with corresponding ideality factors.



Thermal treatment above 350°C was found to have reduced performance in current density where crystal phase changes begin to occur. The rectification ratio,  $I_F/I_R$ , for the as-deposited was found to be 1015 and thermally treated samples at 350°C and 400°C were found to be 3294 and 552, respectively.

Nonstoichiometric, reduced  $TiO_2$  samples were found to have a smaller built-in voltage and improved ideality factors. However, thermally treated nonstoichiometric diodes exhibited a shunt conductance regime and a lower current density (Figure 4-20). It is important to note that a post-thermal treatment reduced the reverse bias current leakage by about two-orders of magnitude for both stoichiometric and nonstoichiometric devices. The  $I_F/I_R$  ratio for the as-deposited, 350°C, and 400°C samples were 8, 82, and 144, respectively. We can see that the rectification is much lower compared to the stoichiometric samples by a factor of  $10^2$ .

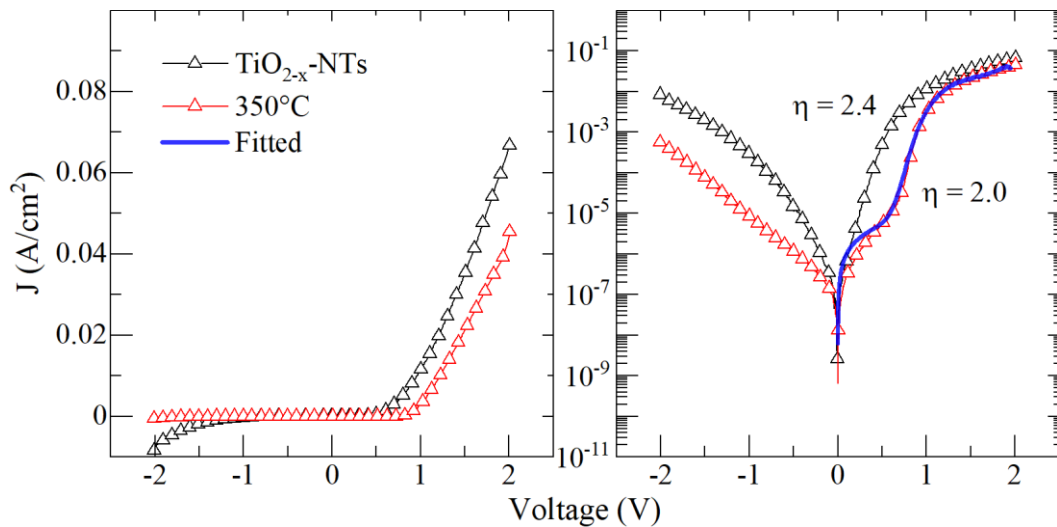


Figure 4-20: (a) Current-Voltage characteristics of nonstoichiometric  $TiO_2$ -NT Schottky diodes for the as-deposited Pt and thermally treated diodes. (b) Semi-log plot with corresponding ideality factors and fitted curve (blue).

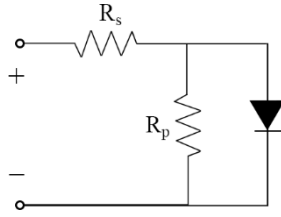


Figure 4-21: Equivalent circuit with a parallel, or shunt, conduction path.

The shunt path can be modeled using the equivalent circuit found in Figure 4-21 where the characteristic equation can be found using Kirchhoff's current law and is as follows.

$$J = J_0 \left[ \exp \left( \frac{q(E_a - JR_s)}{\eta k_B T} \right) - 1 \right] + \frac{E_a - JR_s}{R_p} \quad (4.1)$$

Here, the shunt resistance was fit to the J-V curve in Figure 4-20 and found the parallel resistance,  $R_p$ , to be on the order of  $10^5 \Omega$ .

A combined plot for Norde's method is provided in Figure 4-22, where we can see the V locations to gather the  $F_{\min}$  values the extracted barrier height and series resistances are presented in Tables 4-3 and 4-4.

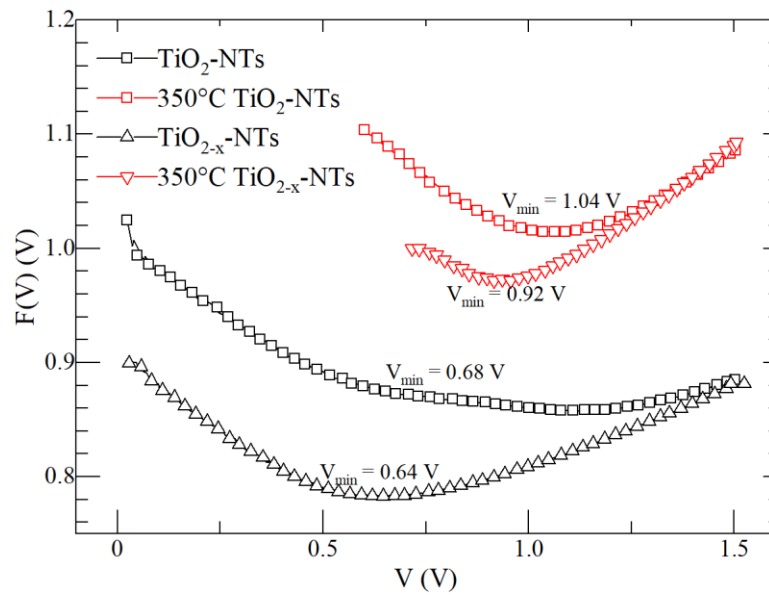


Figure 4-22: Norde's method plot  $F(V)$ - $V$  for both stoichiometric and nonstoichiometric TiO<sub>2</sub>-NT diodes.

Cheung and Cheung's equations are plotted on a double Y axis in Figure 4-23 where the left and right axis correspond to the  $\frac{dV}{d\ln J}$  and  $H(V)$  functions with respect to the current density  $J$ .

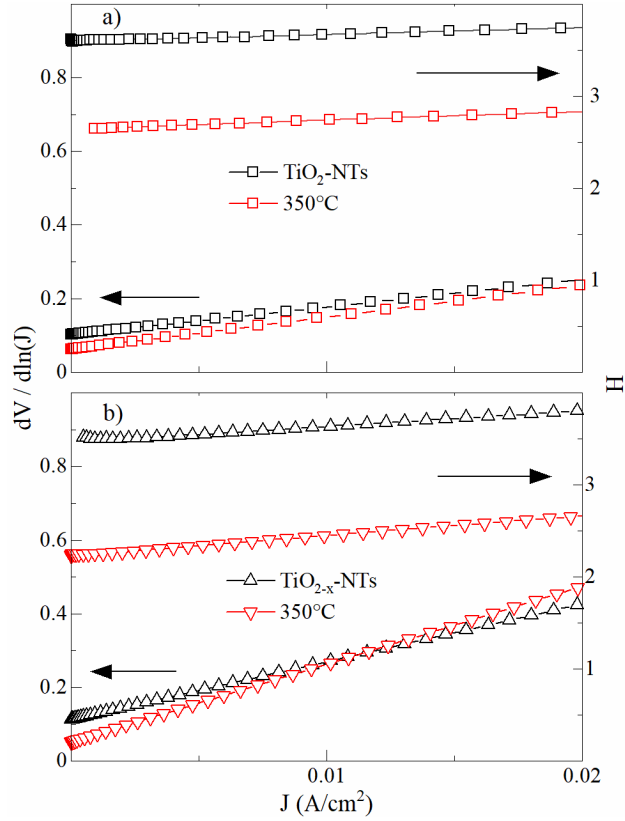


Figure 4-23: Cheung and Cheung's functions plotted for (a) stoichiometric and (b) nonstoichiometric  $\text{TiO}_2$ -NT diodes.

Table 4-3 compares the as-deposited stoichiometric and nonstoichiometric Pt/ $\text{TiO}_2$  Schottky diodes using two Richardson constants of 1200 [ $\text{A}/\text{cm}^2\text{K}^2$ ] and 0.0028 [ $\text{A}/\text{cmK}^{2/3}$ ].

Table 4-3: As deposited Pt/ $\text{TiO}_2$ -NT Schottky diodes.

As Deposited	Richardson Constant	Thermionic Emission Model		Norde's Method		Cheung-Cheung Method		
		$\phi_{\text{sb}}(\text{eV})$	$\eta$	$\phi_{\text{sb}}(\text{eV})$	$R_s(\Omega)$	$\phi_{\text{sb}}(\text{eV})$	$\eta$	$R_s(\Omega)$
Stoichiometric	$A_{3D}^*$	1.07	3.75	1.05	4.74	0.89	3.95	7.50

	$A_{2D}^*$	0.66	3.7	0.64	4.74	0.49	3.95	7.30
Nonstoichiometric	$A_{3D}^*$	1.00	2.4	0.88	12.49	0.63	4.37	16.12
	$A_{2D}^*$	0.59	2.4	0.47	12.49	0.38	4.37	16.12

Table 4-4 compares the post-thermal treatment devices using the two Richardson constants used above.

Table 4-4: Post-thermal treatment Pt/TiO<sub>2</sub>-NT Schottky diodes.

Post-Thermal Treatment	Richardson Constant	Thermionic Emission Model		Norde's Method		Cheung-Cheung Method		
		$\phi_{sb}(eV)$	$\eta$	$\phi_{sb}(eV)$	$R_s(\Omega)$	$\phi_{sb}(eV)$	$\eta$	$R_s(\Omega)$
Stoichiometric	$A_{3D}^*$	1.14	2.04	1.33	14.3	1.1	2.4	9.40
	$A_{2D}^*$	0.72	2.04	0.92	14.32	0.68	2.41	9.40
Nonstoichiometric	$A_{3D}^*$	0.96	2.03	1.25	18.37	1.10	2.01	22.54
	$A_{2D}^*$	0.55	2.03	0.84	18.37	0.69	2.01	22.54

The log-log plot for both stoichiometric and nonstoichiometric samples is shown in Figure 4-24. As previously mentioned, limitations in the 2601A source meter prevented a

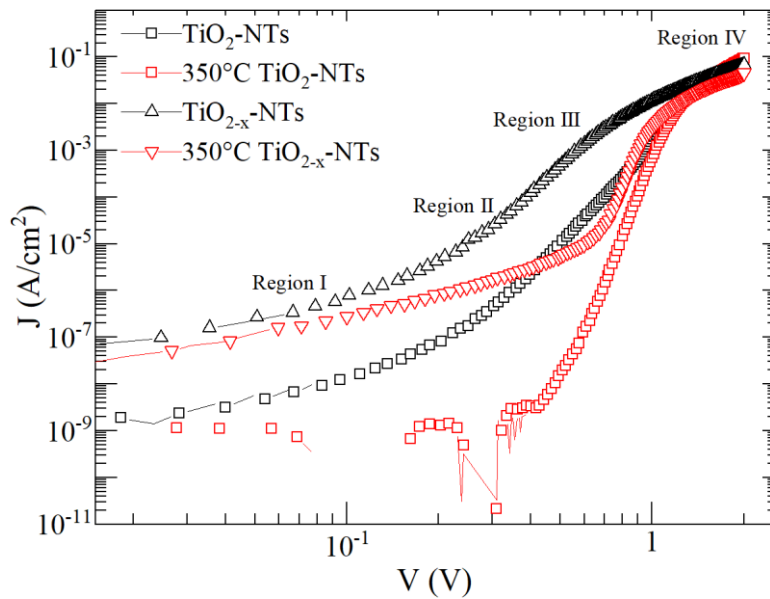


Figure 4-24: Log-Log plot for both stoichiometric and nonstoichiometric TiO<sub>2</sub>-NT diodes.

continuous current measurement for the post-thermally treated stoichiometric sample. Region I, II, III, and IV indicate the ohmic, space charge limited conduction (SCLC), trap-filled limit, and the trap-free SCLC, respectively. The slopes for each region are given in Table 4-5.

Table 4-5: Slopes in each region of the log-log plot.

		<b>Region</b>			
		<b>I</b>	<b>II</b>	<b>III</b>	<b>IV</b>
<b>Stoichiometric</b>	As Deposited	1.59	3.34	7.24	4.44
	Post-Thermal Treatment	0.83	1.98	16.14	6.58
<b>Nonstoichiometric</b>	As Deposited	1.95	4.20	5.92	2.53
	Post-Thermal Treatment	1.20	4.81	12.33	3.28

Trap-limited and space charge limited current (SCLC) is commonly illustrated in a log-log plot due to its power law relationship<sup>82</sup>. Recently, the parameter, G, was introduced to mark transitions of rapidly rising current in the diode J-V conduction curves<sup>83-85</sup>. This metric is defined as:

$$G = \frac{d\log(J)}{d\log(V)} \quad (4.2)$$

where the derivatives are known to have more sensitivity to slope changes. This provides a simple identification of a transition voltage proportional to the built-in potential ( $V_{bi}$ ). Coincidentally, these peaks in the G-V curve indicate a trap-filled limit and a transition into SCLC. Figure 5 presents the log-log J-V and G-V curve for (a) stoichiometric and (b) nonstoichiometric samples before and after thermal treatment. Before thermal annealing, the diodes suggest discrete traps with a concentration density of

$\sim 10^{10} \text{ cm}^{-3}$  at around 0.4 V with a secondary peak indicating the presence of discrete traps of varying concentrations.<sup>84</sup> Post-fabrication annealing shows the trap-filled limit transition peak increased between 0.81 V and 0.83 V for stoichiometric and nonstoichiometric  $\text{TiO}_2$ , respectively. The peak shift from 0.4 V to 0.8 V indicates an increase in trap densities for both devices. It is also worth noting that a post fabrication annealing results in an increase in trap depth as indicated by the downward shift in the log-log curves in Figure 4-25.<sup>86</sup>

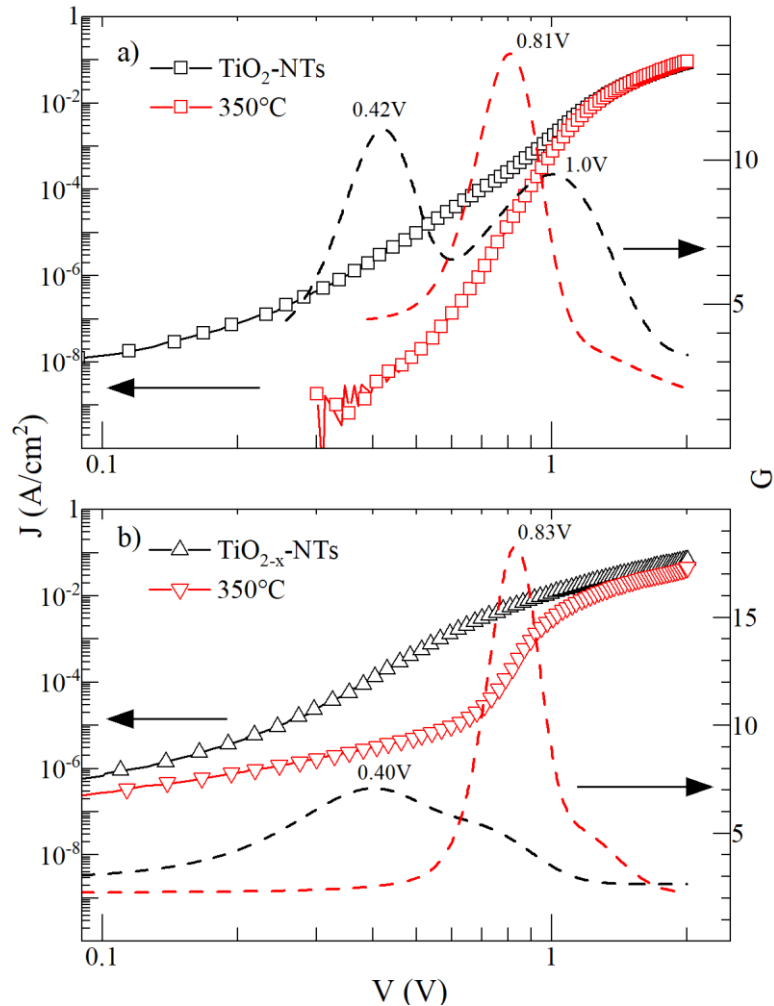


Figure 4-25: Forward bias J-V and G-V curves for (a) stoichiometric and (b) nonstoichiometric samples. G-V characteristics represent the transition voltage between the trap-limited and SCLC regions.

## 4.6 Capacitance – Voltage Characteristics

The C-V measurements of the diode were taken before and after thermal treatment at 50 mV<sub>p-p</sub> and 1 MHz, see Figure 4-26.

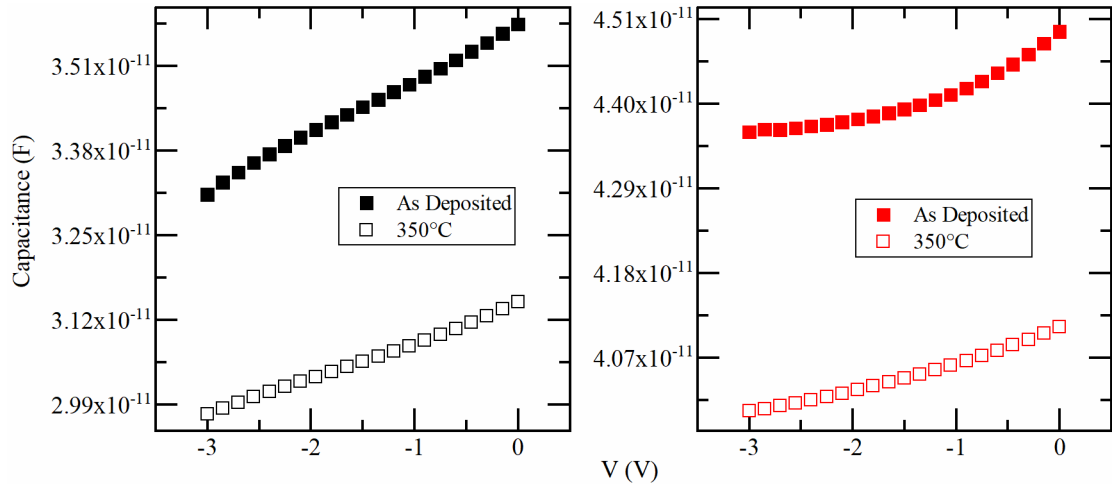


Figure 4-26: Capacitance-Voltage measurements of as-deposited and post-thermally treated stoichiometric and nonstoichiometric TiO<sub>2</sub>-NT Schottky diodes.

For common, non-resistive, diodes, the C-V plots can be used to determine electronic parameters such as the built-in voltage, the carrier concentration, depletion widths, and Schottky barrier height. In this material, however, the C-V measurements at 1MHz displayed little variation in capacitance values which led to incorrect extractions of electronic parameters. The built-in voltage can be obtained by taking the  $1/C^2$  plot and linearly fitting the curve and determining where the line crosses the x-axis. This measurement resulted in a built-in voltage of 10<sup>-11</sup> V which does not match the J-V characteristics. Due to limitations, we were unable to capture lower frequency values which may have provided us with a more accurate capacitance-voltage measurement.

## 5 CONCLUSION & FUTURE WORK

### 5.1 Conclusion

The improvements in microelectronic fabrication processes have dramatically increased over the past two decades allowing for a more precise control over nanostructure geometries. Stoichiometric TiO<sub>2</sub>-NTs can be easily fabricated with high geometric precision and can be tuned for a variety of applications. This thesis described the experiments performed to synthesize highly ordered TiO<sub>2</sub>-NT arrays using electrochemical anodization. We discover that a perfect and sensitive balance between the NH<sub>4</sub>F, water concentration, recrystallization parameters is necessary to develop a uniformly arranged nanostructure. The stoichiometric and nonstoichiometric TiO<sub>2</sub>-NTs were coated with Pt, forming a conformal Schottky barrier where a current rectification behavior was observed between the anode and cathode. The metal contact deposition required enough time to diffuse into the porous structure as well as a high enough precursor concentration to ensure a conformal coating.

Material characterization techniques such as XRD and SEM showed that the crystal structure was predominantly in the anatase phase and that the surface quality improved after changing anodization and annealing parameters. Annealing TiO<sub>2</sub> in a vacuum environment was discovered to create a new parallel resistance behavior in the material attributed to oxygen vacancies. The electrical measurements, such as I-V and C-V, were applied to both stoichiometric and nonstoichiometric TiO<sub>2</sub> diodes. The M-S diode parameters such as the Schottky barrier height, ideality factors, and series resistances were



extracted from the I-V measurements using thermionic emission equations, Cheung-Cheung's method, as well as Norde's method.

The electrical characteristics of stoichiometric TiO<sub>2</sub>-NT diodes displayed a rectification ratio by three orders of magnitude for both as-deposited and post-annealed samples. Reverse bias current was found to be improved by two orders of magnitude after a thermal treatment. The nonstoichiometric diodes, however, showed a more resistive behavior with only one to two orders of magnitude for the as deposited and post-annealed samples, respectively. A parallel, or shunt, resistance was formed in the post-annealed, nonstoichiometric samples indicating that ohmic conduction occurs before the turn-on voltage.

## **5.2 Future Work**

Nonstoichiometric TiO<sub>2</sub> diodes exhibit a resistive switching, or memristor, behavior due to the V<sub>o</sub> sites, a behavior that biological dendrites and neurons exhibit. Memristor applications are slowly integrating into the field of neuromorphic computing for artificial intelligence algorithms. Additional experiments are needed to understand and control the location of V<sub>o</sub> sites in anatase TiO<sub>2</sub> materials to develop a reproducible fabrication process. There are still many unknowns in nonstoichiometric TiO<sub>2</sub> that are waiting to be discovered and can significantly improve future technologies. Another area to investigate is the mechanism behind the fluorine ions during the annealing process. When annealed in a closed environment after electrochemically anodizing, fluorine ions appear to remain within the crystal. Fluorine ions can be considered a dopant, providing more electrons through either interstitial or substitutional defects.

Our current understanding of parasitic capacitance and resistances in conformal M-S interfaces requires further understanding. The capacitance and parallel resistances along the NT walls and at the bottom play different roles in the conduction process that has yet to be characterized for conformal barriers on TiO<sub>2</sub>-NTs.

## APPENDIX

### I. Reverse Saturation Current Density

The current density flowing out of a surface in the z-direction is given by

$$J_0 = 2q \left( \frac{m^*}{2\pi\hbar} \right)^N v_z dv_x dv_y dv_z \cdot \exp(E_F/k_B T) \cdot \exp\left(-m^*(v_x^2 + v_y^2 + v_z^2)/2k_B T\right) \quad (I.1)$$

where  $m^*$ ,  $N$ ,  $\hbar$ ,  $v$ , and  $E_F$  are the effective mass, dimensionality, Planck's constant, velocities, and Fermi energy, respectively. For bulk, macroscale semiconductors the dimensionality is 3 (3D) and the components  $v_x$  and  $v_y$  both contribute to the current flux.

By using the integration identities

$$\int_{-\infty}^{\infty} \exp(-av^2) dv = \sqrt{\frac{\pi}{a}} \quad (I.2)$$

$$\int_{v_{z,0}}^{\infty} v_z \cdot \exp(-mv_z^2) \cdot dz = \frac{k_B T}{m^*} \cdot \exp\left(-\frac{(E_F + \phi_{sb})}{k_B T}\right) \quad (I.3)$$

we obtain a 3D saturation current density of

$$J_{0,3D} = \frac{4q\pi m^* k_B^2}{h^3} \cdot T^2 \cdot \exp^{-\phi_{sb}/k_B T} \quad (I.4)$$

where the first term is typically denoted as the variable  $A^*$ , the Richardson constant, with units of  $[A/m^2 K^2]$ .

For two-dimensions, only one other  $v$  component contributes to the transmission equation and is characterized by the following equation.

$$J_{0,2D} = \frac{q}{h^2} \sqrt{8\pi m^* k_B^3} \cdot T^{3/2} \cdot \exp^{-\phi_{sb}/k_B T} \quad (I.5)$$

It is important to note the units of  $A^*$  are  $[A/mK^{3/2}]$ .

## II. Linear Least-Squares Regression Algorithm

Variables  $x$  and  $y$  indicate voltage and current measurements, respectively.

$$n = \text{length}(x);$$

$$\text{sumx} = \text{sum}(x);$$

$$\text{sumxx} = \text{sum}(x.*x);$$

$$\text{sumxy} = \text{sum}(x.*y);$$

$$\text{sumy} = \text{sum}(y);$$

$$D = n*\text{sumxx} - \text{sumx}^2;$$

$$a0 = (\text{sumxx}*\text{sumy} - \text{sumxy}*\text{sumx})/D;$$

$$a1 = (n*\text{sumxy} - \text{sumx}*\text{sumy})/D;$$

## REFERENCES

- (1) Sumlo Iijima. Helical Microtubules of Graphitic Carbon. *Nature* **1991**, 354 (354), 56–58.
- (2) Ashcroft, N. W.; Mermin, N. D. *Solid State Physics*; Company, B. P., Ed.; Holt, Rinehart and Winston, 1976.
- (3) Chen, G. *Nanoscale Energy Transport and Conversion*; Oxford University Press, 2005.
- (4) Neamen, D. A. *Semiconductor Physics and Devices*, 4th ed.; The McGraw-Hill Companies, 2012.
- (5) Fujishima, A.; Kenichi, H. Electrochemical Photolysis of Water at a Semiconductor Electrode. *Nature* **1972**, 238 (5358), 38–40.
- (6) Fujishima, A.; Rao, T. N.; Tryk, D. A. *Titanium Dioxide Photocatalysis*; 2000; Vol. 1.
- (7) Fujishima, A.; Zhang, X. Titanium Dioxide Photocatalysis: Present Situation and Future Approaches. *Comptes Rendus Chim.* **2006**, 9 (5–6), 750–760.
- (8) Luttrell, T.; Halpegamage, S.; Tao, J.; Kramer, A.; Sutter, E.; Batzill, M. Why Is Anatase a Better Photocatalyst than Rutile? - Model Studies on Epitaxial TiO<sub>2</sub> Films. *Sci. Rep.* **2015**, 4, 1–8.
- (9) Zhang, Z.; Gong, Z.; Yang, Y. Electrochemical Performance and Surface Properties of Bare and TiO<sub>2</sub>-Coated Cathode Materials in Lithium-Ion Batteries. *J. Phys. Chem. B* **2004**, 108, 17546–17552.
- (10) Lin, C. W.; Hung, C. L.; Venkateswarlu, M.; Hwang, B. J. Influence of TiO<sub>2</sub> Nano-Particles on the Transport Properties of Composite Polymer Electrolyte for Lithium-Ion Batteries. *J. Power Sources* **2005**, 146 (1–2), 397–401.
- (11) Wang, Q.; Wen, Z.; Li, J. Solvent-Controlled Synthesis and Electrochemical Lithium Storage of One-Dimensional TiO<sub>2</sub> Nanostructures. *Inorg. Chem.* **2006**, 45, 6944–6949.
- (12) Zhang, Q.; Chen, R.; San, H.; Liu, G.; Wang, K. Betavoltaic Microbatteries Using TiO<sub>2</sub> Nanotube Arrays. *2015 Transducers - 2015 18th Int. Conf. Solid-State Sensors, Actuators Microsystems, TRANSDUCERS 2015* **2015**, 1909–1912.
- (13) Wang, Z.; Chen, G.; Xia, D.; Zhang, L. Studies on the Electrocatalytic Properties of PtRu/C-TiO<sub>2</sub> toward the Oxidation of Methanol. *J. Alloys Compd.* **2008**, 450 (1–2), 148–151.

- (14) Herrero, E.; Franaszczuk, K.; Wieckowski, A. Electrochemistry of Methanol at Low Index Crystal Planes of Platinum: An Integrated Voltammetric and Chronoamperometric Study. *J. Phys. Chem.* **2002**, *98* (19), 5074–5083.
- (15) Trapalis, C. C.; Keivanidis, P.; Kordas, G.; Zaharescu, M.; Crisan, M.; Szatvanyi, A.; Gartner, M. TiO<sub>2</sub>(Fe<sup>3+</sup>) Nanostructured Thin Films with Antibacterial Properties. *Thin Solid Films* **2003**, *433* (1-2 SPEC.), 186–190.
- (16) Tennakone, K.; Wijayantha, K. G. U. Heavy-Metal Extraction from Aqueous Medium with an Immobilized TiO<sub>2</sub> Photocatalyst and a Solid Sacrificial Agent. *J. Photochem. Photobiol. A Chem.* **1998**, *113* (1), 89–92.
- (17) Ji, X.; Zuppero, A.; Gidwani, J. M.; Somorjai, G. A. The Catalytic Nanodiode: Gas Phase Catalytic Reaction Generated Electron Flow Using Nanoscale Platinum Titanium Oxide Schottky Diodes. *Nano Lett.* **2005**, *5* (4), 753–756.
- (18) Francioso, L.; Presicce, D. S.; Epifani, M.; Siciliano, P.; Ficarella, A. Response Evaluation of TiO<sub>2</sub> Sensor to Flue Gas on Spark Ignition Engine and in Controlled Environment. *Sensors Actuators, B Chem.* **2005**, *107* (2), 563–571.
- (19) Haghghat, F.; Khodadadi, A.; Mortazavi, Y. Temperature-Independent Ceria- and Pt-Doped Nano-Size TiO<sub>2</sub> Oxygen Lambda Sensor Using Pt/SiO<sub>2</sub> Catalytic Filter. *Sensors Actuators, B Chem.* **2008**, *129* (1), 47–52.
- (20) Selman, A. M.; Husham, M. Calcination Induced Phase Transformation of TiO<sub>2</sub> Nanostructures and Fabricated a Schottky Diode as Humidity Sensor Based on Rutile Phase. *Sens. Bio-Sensing Res.* **2016**, *11*, 8–13.
- (21) Funk, S.; Hokkanen, B.; Burghaus, U.; Ghicov, A.; Schmuki, P. Unexpected Adsorption of Oxygen on TiO<sub>2</sub> Nanotube Arrays: Influence of Crystal Structure. *Nano Lett.* **2007**, *7* (4), 1091–1094.
- (22) Eftekhari, A.; Fang, B. Electrochemical Hydrogen Storage: Opportunities for Fuel Storage, Batteries, Fuel Cells, and Supercapacitors. *Int. J. Hydrogen Energy* **2017**, *42* (40), 25143–25165.
- (23) An, L.; Zhao, T.; Yan, X.; Zhou, X.; Tan, P. The Dual Role of Hydrogen Peroxide in Fuel Cells. *Sci. Bull.* **2015**, *60* (1), 55–64.
- (24) Abdullah, N.; Kamarudin, S. K. Titanium Dioxide in Fuel Cell Technology: An Overview. *J. Power Sources* **2015**, *278* (September 2019), 109–118.
- (25) Kang, X.; Liu, S.; Dai, Z.; He, Y.; Song, X.; Tan, Z. *Titanium Dioxide: From Engineering to Applications*; 2019; Vol. 9.
- (26) Abdullah, M.; Kamarudin, S. K. Titanium Dioxide Nanotubes (TNT) in Energy and Environmental Applications: An Overview. *Renew. Sustain. Energy Rev.* **2017**, *76* (February 2016), 212–225.

- (27) Lee, W. J.; Lim, D. H.; Smyrl, W. H. Miniature H<sub>2</sub>/O<sub>2</sub> Fuel Cells Using TiO<sub>2</sub> Nanotube Substrates and Sputtered Pt Catalyst. *J. Power Sources* **2013**, *240*, 612–617.
- (28) Frank, A. J.; Kopidakis, N.; Lagemaat, J. Van De. Electrons in Nanostructured TiO<sub>2</sub> Solar Cells: Transport, Recombination and Photovoltaic Properties. *Coordination Chemistry Reviews*. Elsevier July 1, 2004, pp 1165–1179.
- (29) Grätzel, M. Conversion of Sunlight to Electric Power by Nanocrystalline Dye-Sensitized Solar Cells. *J. Photochem. Photobiol. A Chem.* **2004**, *164* (1–3), 3–14.
- (30) Cheng, X.; Zhang, Y.; Bi, Y. Spatial Dual-Electric Fields for Highly Enhanced the Solar Water Splitting of TiO<sub>2</sub> Nanotube Arrays. *Nano Energy* **2019**, *57* (December 2018), 542–548.
- (31) Guo, W.; Xue, X.; Wang, S.; Lin, C.; Wang, Z. L. An Integrated Power Pack of Dye-Sensitized Solar Cell and Li Battery Based on Double-Sided TiO<sub>2</sub> Nanotube Arrays. *Nano Lett.* **2012**, *12* (5), 2520–2523.
- (32) Zhang, L.; Chen, Z.; Joshua Yang, J.; Wysocki, B.; McDonald, N.; Chen, Y. A Compact Modeling of TiO<sub>2</sub>-TiO<sub>2-x</sub> Memristor. *Appl. Phys. Lett.* **2013**, *102* (15).
- (33) Khot, A. C.; Desai, N. D.; Khot, K. V.; Salunkhe, M. M.; Chougule, M. A.; Bhave, T. M.; Kamat, R. K.; Musselman, K. P.; Dongale, T. D. Bipolar Resistive Switching and Memristive Properties of Hydrothermally Synthesized TiO<sub>2</sub> Nanorod Array: Effect of Growth Temperature. *Mater. Des.* **2018**, *151*, 37–47.
- (34) Mohanty, S. P. Memristor: From Basics to Deployment. *IEEE Potentials* **2013**, *32* (3), 34–39.
- (35) Mettan, X.; Jaćimović, J.; Barišić, O. S.; Pisoni, A.; Batistić, I.; Horváth, E.; Brown, S.; Rossi, L.; Szirmai, P.; Farkas, B.; Berger, H.; Forró, L. Tailoring Thermal Conduction in Anatase TiO<sub>2</sub>. *Commun. Phys.* **2019**, *2* (1), 1–7.
- (36) Zayer, F.; Dghais, W.; Belgacem, H. TiO<sub>2</sub> Memristor Model-Based Chaotic Oscillator. *IEEE* **2017**, No. 2, 54–57.
- (37) Jeong, D. S.; Schroeder, H.; Waser, R. Abnormal Bipolar-like Resistance Change Behavior Induced by Symmetric Electroforming in Pt/TiO<sub>2</sub>/Pt Resistive Switching Cells. *Nanotechnology* **2009**, *20* (37).
- (38) Sulka, G. D.; Kapusta-Kołodziej, J.; Brzózka, A.; Jaskuła, M. Fabrication of Nanoporous TiO<sub>2</sub> by Electrochemical Anodization. *Electrochim. Acta* **2010**, *55* (14), 4359–4367.
- (39) Asoh, H.; Ishino, M.; Hashimoto, H. AC-Bipolar Anodization of Aluminum: Effects of Frequency on Thickness of Porous Alumina Films. *J. Electrochem. Soc.* **2018**, *165* (7), C295–C301.

- (40) Ren, L.; Li, Y.; Hou, J.; Zhao, X.; Pan, C. Preparation and Enhanced Photocatalytic Activity of TiO<sub>2</sub> Nanocrystals with Internal Pores. *ACS Appl. Mater. Interfaces* **2014**, *6* (3), 1608–1615.
- (41) Kowalski, D.; Kim, D.; Schmuki, P. TiO<sub>2</sub> Nanotubes, Nanochannels and Mesosponge: Self-Organized Formation and Applications. *Nano Today* **2013**, *8* (3), 235–264.
- (42) Sun, L.; Zhang, S.; Sun, X. W.; Wang, X.; Cai, Y. Double-Sided Anodic Titania Nanotube Arrays: A Lopsided Growth Process. *Langmuir* **2010**, *26* (23), 18424–18429.
- (43) Wang, D. W.; Fang, H. T.; Li, F.; Chen, Z. G.; Zhong, Q. S.; Lu, G. Q.; Cheng, H. M. Aligned Titania Nanotubes as an Intercalation Anode Material for Hybrid Electrochemical Energy Storage. *Adv. Funct. Mater.* **2008**, *18* (23), 3787–3793.
- (44) Roy, P.; Berger, S.; Schmuki, P.; Schmuki, P. TiO<sub>2</sub> Nanotubes: Synthesis and Applications Reviews. *Angew. Chemie* **2011**, *50*, 2904–2939.
- (45) Song, J.; Zheng, M.; Zhang, B.; Li, Q.; Wang, F.; Ma, L.; Li, Y.; Zhu, C.; Ma, L.; Shen, W. Fast Growth of Highly Ordered TiO<sub>2</sub> Nanotube Arrays on Si Substrate under High-Field Anodization. *Nano-Micro Lett.* **2017**, *9* (2).
- (46) Kang, T. S.; Smith, A. P.; Taylor, B. E.; Durstock, M. F. Fabrication of Highly-Ordered TiO<sub>2</sub> Nanotube Arrays and Their Use in Dye-Sensitized Solar Cells. *Nano Lett.* **2009**, *9* (2), 601–606.
- (47) Loget, G.; So, S.; Hahn, R.; Schmuki, P. Bipolar Anodization Enables the Fabrication of Controlled Arrays of TiO<sub>2</sub> Nanotube Gradients. *J. Mater. Chem. A* **2014**, *2* (42), 17740–17745.
- (48) Raja, K. S.; Gandhi, T.; Misra, M. Effect of Water Content of Ethylene Glycol as Electrolyte for Synthesis of Ordered Titania Nanotubes. *Electrochem. commun.* **2007**, *9* (5), 1069–1076.
- (49) Kim, J.; Kim, B.; Oh, C.; Ryu, J.; Kim, H.; Park, E.; No, K.; Hong, S. Effects of NH<sub>4</sub>F and Distilled Water on Structure of Pores in TiO<sub>2</sub> Nanotube Arrays. *Sci. Rep.* **2018**, *8* (1), 12487.
- (50) Acevedo-Peña, P.; Lartundo-Rojas, L.; González, I. Effect of Water and Fluoride Content on Morphology and Barrier Layer Properties of TiO<sub>2</sub> Nanotubes Grown in Ethylene Glycol-Based Electrolytes. *J. Solid State Electrochem.* **2013**, *17* (11), 2939–2947.
- (51) Xiong, L. Bin; Li, J. L.; Yang, B.; Yu, Y. Ti<sup>3+</sup> in the Surface of Titanium Dioxide: Generation, Properties and Photocatalytic Application. *J. Nanomater.* **2012**, 2012.
- (52) Nah, Y. C.; Paramasivam, I.; Schmuki, P. Doped TiO<sub>2</sub> and TiO<sub>2</sub> Nanotubes:



Synthesis and Applications. *ChemPhysChem* **2010**, *11* (13), 2698–2713.

- (53) Alexander, J. C. *Defect Chemistry of TiO<sub>2</sub> and Phase Diagrams of TiO<sub>2</sub> and H<sub>2</sub>O*; 2016.
- (54) Hou, Q. Y.; Wu, Y. G. R. Le; Zhao, C. W. Effects of the Concentration of Heavily Oxygen Vacancy of Rutile TiO<sub>2</sub> on Electric Conductivity Performance from First Principles Study. *Wuli Xuebao/Acta Phys. Sin.* **2013**, *62* (16), 1–6.
- (55) Cheng, Z.; Liu, T.; Yang, C.; Gan, H.; Zhang, F.; Chen, J. Study on the Electronic Structures of the Reduced Anatase TiO<sub>2</sub> by the First-Principle Calculation. *J. Phys. Chem. Solids* **2012**, *73* (2), 302–307.
- (56) Knez, D.; Dražić, G.; Chaluvadi, S. K.; Orgiani, P.; Fabris, S.; Panaccione, G.; Rossi, G.; Ciancio, R. Unveiling Oxygen Vacancy Superstructures in Reduced Anatase Thin Films. *Nano Lett.* **2020**, *20* (9), 6444–6451.
- (57) Langhammer, D.; Thyr, J.; Österlund, L. Surface Properties of Reduced and Stoichiometric TiO<sub>2</sub> As Probed by SO<sub>2</sub> Adsorption. *J. Phys. Chem. C* **2019**, *123* (40), 24549–24557.
- (58) Pura, A.; Rubenis, K.; Stepanovs, D.; Berzina-Cimdina, L.; Ozolins, J. Semiconducting Properties of Nonstoichiometric TiO<sub>2-x</sub> Ceramics. *Process. Appl. Ceram.* **2012**, *6* (2), 91–95.
- (59) Pan, X.; Yang, M. Q.; Fu, X.; Zhang, N.; Xu, Y. J. Defective TiO<sub>2</sub> with Oxygen Vacancies: Synthesis, Properties and Photocatalytic Applications. *Nanoscale* **2013**, *5* (9), 3601–3614.
- (60) Wajid Shah, M.; Zhu, Y.; Fan, X.; Zhao, J.; Li, Y.; Asim, S.; Wang, C. Facile Synthesis of Defective TiO<sub>2-x</sub> Nanocrystals with High Surface Area and Tailoring Bandgap for Visible-Light Photocatalysis. *Sci. Rep.* **2015**, *5* (October).
- (61) Millot, F.; Picard, C. Oxygen Self-Diffusion in Non-Stoichiometric Rutile TiO<sub>2-x</sub> at High Temperature. *Solid State Ionics* **1988**, No. 28–30, 1344–1348.
- (62) Lim, S. M.; Yeon, H. W.; Lee, G. B.; Jin, M. G.; Lee, S. Y.; Jo, J.; Kim, M.; Joo, Y. C. Thermally Stable Amorphous Oxide-Based Schottky Diodes through Oxygen Vacancy Control at Metal/Oxide Interfaces. *Sci. Rep.* **2019**, *9* (1), 1–9.
- (63) Valeeva, A. A.; Kozlova, E. A.; Vokhmintsev, A. S.; Kamalov, R. V.; Dorosheva, I. B.; Saraev, A. A.; Weinstein, I. A.; Rempel, A. A. Nonstoichiometric Titanium Dioxide Nanotubes with Enhanced Catalytical Activity under Visible Light. *Sci. Rep.* **2018**, *8* (1), 1–10.
- (64) Jackman, M. J.; Thomas, A. G.; Muryn, C. Photoelectron Spectroscopy Study of Stoichiometric and Reduced Anatase TiO<sub>2</sub> (101) Surfaces: The Effect of Subsurface Defects on Water Adsorption at Near-Ambient Pressures. *J. Phys.*

*Chem. C* **2015**, *119* (13682–13690).

- (65) Das, D.; Barman, A.; Kumar, S.; Sinha, A. K.; Gupta, M.; Singhal, R.; Johari, P.; Kanjilal, A. Synergistic Effect of Singly Charged Oxygen Vacancies and Ligand Field for Regulating Transport Properties of Resistive Switching Memories. *J. Phys. Chem. C* **2019**, *123*, 26812–26822.
- (66) Braun, F. Ueber Die Stromleitung Durch Schwefelmetalle. *Ann. der Phys. und Chemie* **1874**, *153* (4), 556–563.
- (67) Schottky, W. Halbleitertheorie Der Sperrschicht. *Naturwissenschaften* **1938**, *26*, 843.
- (68) Mott, N. F. Note on the Contact between a Metal and an Insulator or Semiconductor. *Math. Proc. Cambridge Philos. Soc.* **1938**, *34* (4), 568–572.
- (69) Tyagi, M. S. Physics of Schottky Barrier Junctions. In *Metal-Semiconductor Schottky Barrier Junctions and Their Applications*; Springer US, 1984; pp 1–60.
- (70) Campbell, S. A. *Fabrication Engineering at the Micro- and Nanoscale*, 4th ed.; Oxford University Press, 2013.
- (71) Klaus, J. W.; Ferro, S. J.; George, S. M. Atomic Layer Deposition of Tungsten Using Sequential Surface Chemistry with a Sacrificial Stripping Reaction. *Thin Solid Films* **2000**, *360* (1–2), 145–153.
- (72) Gordon, R. G.; Hausmann, D.; Kim, E.; Shepard, J. A Kinetic Model for Step Coverage by Atomic Layer Deposition in Narrow Holes or Trenches. *Chem. Vapor Depos.* **2003**, *9* (2), 73–78.
- (73) Dendooven, J.; Devloo-Casier, K.; Ide, M.; Grandfield, K.; Kurttepel, M.; Ludwig, K. F.; Bals, S.; Van Der Voort, P.; Detavernier, C. Atomic Layer Deposition-Based Tuning of the Pore Size in Mesoporous Thin Films Studied by in Situ Grazing Incidence Small Angle X-Ray Scattering. *Nanoscale* **2014**, *6* (24), 14991–14998.
- (74) Yazdani, N.; Chawla, V.; Edwards, E.; Wood, V.; Park, H. G.; Utke, I. Modeling and Optimization of Atomic Layer Deposition Processes on Vertically Aligned Carbon Nanotubes. *Beilstein J. Nanotechnol.* **2014**, *5* (1), 234–244.
- (75) Knoops, H. C. M.; Potts, S. E.; Bol, A. A.; Kessels, W. M. M. 27 - Atomic Layer Deposition. In *Handbook of Crystal Growth (Second Edition)*; Kuech, T. F., Ed.; Handbook of Crystal Growth; North-Holland: Boston, 2015; pp 1101–1134.
- (76) Zhang, S.; Li, L.; Kumar, A. *Material Characterization Techniques*; Taylor & Francis Group, 2009.
- (77) Norde, H. A Modified Forward I-V Plot for Schottky Diodes with High Series

- Resistance. *J. Appl. Phys.* **1979**, *50* (7), 5052–5053.
- (78) Cheung, S. K.; Cheung, N. W. Extraction of Schottky Diode Parameters from Forward Current-Voltage Characteristics. *Appl. Phys. Lett* **1986**, *49* (2), 85–87.
- (79) Esfandiari, R. S. *Numerical Methods for Engineers and Scientists Using MATLAB*; Taylor & Francis Group, 2017.
- (80) Beyer, G.; Satta, A.; Schuhmacher, J.; Maex, K.; Besling, W.; Kilpela, O.; Sprey, H.; Tempel, G. Development of Sub-10-Nm Atomic Layer Deposition Barriers for Cu/Low-k Interconnects. *Microelectron. Eng.* **2002**, *64* (1–4), 233–245.
- (81) Chen, X.; Liu, L.; Yu, P. Y.; Mao, S. S. Increasing Solar Absorption for Photocatalysis with Black Hydrogenated Titanium Dioxide Nanocrystals. *Science* (80-. ). **2011**, *331* (6018), 746–750.
- (82) Jain, A.; Kumar, P.; Jain, S. C.; Kumar, V.; Kaur, R.; Mehra, R. M. Trap Filled Limit Voltage (VTFL) and V<sup>2</sup> Law in Space Charge Limited Currents. *J. Appl. Phys.* **2007**, *102* (9).
- (83) Mantri, P.; Rizvi, S. M. H.; Mazhari, B. Estimation of Built-in Voltage from Steady-State Current-Voltage Characteristics of Organic Diodes. *Org. Electron.* **2013**, *14* (8), 2034–2038.
- (84) Rizvi, S. M. H.; Mantri, P.; Mazhari, B. Traps Signature in Steady State Current-Voltage Characteristics of Organic Diode. *J. Appl. Phys.* **2014**, *115*, 244502.
- (85) Rogala, M.; Bihlmayer, G.; Dabrowski, P.; Rodenbücher, C.; Wrana, D.; Krok, F.; Klusek, Z.; Szot, K. Self-Reduction of the Native TiO<sub>2</sub> (110) Surface during Cooling after Thermal Annealing – in-Operando Investigations. *Sci. Rep.* **2019**, *9* (1), 1–9.
- (86) Jung, J. H.; Kim, T. W. The Effect of the Trap Density and Depth on the Current Bistability in Organic Bistable Devices. *J. Appl. Phys.* **2011**, *110* (4), 043721.